RESEARCH ARTICLE

Depleting the action of EZH2 through PI3K-mTOR inhibition to overcome metastasis and immunotherapy resistance in triple-negative breast cancer

Michelle Melino[1†], Wen Juan Tu[1†], Helle Bielefeldt-Ohmann[2,3], Martina Proctor[1], Taniya Ahuja[1], John Vandermeide[1], Amanda L. Bain[1], Gahyathiri Nallan[1], Sal Lee Goh[1], Thiru Prasanna[4,5], Jane E. Dahlstrom[6,7], Mariska Miranda[1], Ramesh Kumar Chaudhary[8], Aravind Anandam[8], Sumit Chaudhary[8], Jonathan T. Seal[9], Debottam Sinha[10], Shaoqian Zhang[11], Tam H. Nguyen[12], Sriganesh Srihari[13], Gunter Hartel[14,15], Amy Ives[16], Laeeq Malik[4], Desmond Yip[4,6], Michelle Nottage[16], Melissa Eastgate[16,17] and Sudha Rao[1*]

Running title: *PI3K-mTOR pathway epigenetic switch in TNBC*

[1] Gene Regulation and Translational Medicine Laboratory, QIMR Berghofer Medical Research Institute, Brisbane, QLD, Australia

[2] School of Chemistry and Molecular Biosciences, The University of Queensland, Brisbane, Queensland, Australia

[3] Australian Infectious Diseases Research Centre, Brisbane, Queensland, Australia

[4] Department of Medical Oncology, The Canberra Hospital, Garran, ACT, Australia

[5] Australian National University, Canberra, ACT, Australia

[6] School of Medicine and Psychology, Australian National University, Canberra, ACT, Australia

[7]ACT Pathology, The Canberra Hospital, Canberra Health Services, Garran, ACT, Australia

[8]Department of In Vivo Pharmacology, Biology, Sai Life Sciences, Hyderabad, India

[9] Medicinal Chemistry, Sai Life Sciences Ltd, Manchester, Block 33 Alderley Park, Macclesfield, SK10 4TG, UK.

[10] Faculty of Medicine, Frazer Institute, The University of Queensland, Brisbane, QLD, Australia

[11]Akoya Biosciences, Marlborough, USA

[12] Flow cytometry and Imaging Facility, QIMR Berghofer Medical Research Institute, Brisbane, QLD, Australia

[13] Tumour Immunology, QIMR Berghofer Medical Research Institute, Brisbane, QLD, Australia

[14] Statistics, QIMR Berghofer Medical Research Institute, Brisbane, QLD, Australia

[15] Institute for Biomedicine and Glycomics, Griffith University, Queensland, Australia

[16] Department of Medical Oncology, Royal Brisbane and Women's Hospital, Brisbane, QLD, Australia

[17] Faculty of Medicine, University of Queensland, Herston, QLD 4006, Australia

[†] These authors contributed equally to this work.

*** Correspondence**:

Professor Sudha Rao

Department of Cancer

QIMR Berghofer Medical Research Institute

300 Herston Road

Herston QLD 4006 AUSTRALIA

Email: sudha.rao@qimrberghofer.edu.au

Phone: +61 7 3362 0222

CONFLICTS OF INTEREST

The authors declare no potential conflicts of interest.

ABSTRACT

Almost half of patients with triple-negative breast cancer (TNBC) develop distant metastases, heralding unfavorable outcomes. Here we provide novel insights into the contribution of the PI3K-mTOR pathway to the TNBC phenotypes that promote growth, migration, metastasis, and therapy resistance. Specifically, we demonstrate that dual targeting of PI3K and mTOR but not PI3K alone inhibits cancer cell proliferation and migration *in vitro*. Dual PI3K-mTOR inhibition with paxalisib not only promotes a favorable mesenchymal to epithelial phenotype but also inhibits signatures associated with MICs, including the highly aggressive CSC phenotype, persister cancer cell phenotype (p65, FOXQ1, NRF2, NNMT), and a cancer drug resistance signature (ABCB5, SNAIL, ALDH1). *In vivo*, paxalisib overcomes immunotherapy resistance to reduce primary tumor burden, circulating tumor cells, and direct and indirect indicators of metastasis with a favorable toxicity profile. Gene expression and spatial analyses show that paxalisib profoundly affects the immune microenvironment in tumors, reducing adaptive immune phenotypes associated with immunotherapy resistance (exhausted T cells, Tregs) and pro-tumor innate immune populations such as mast cells. PI3K-mTOR blockade acts upstream of EZH2, impacting both the classical repressive catalytic p85β-EZH2-H27ME3 and active EZH2-NFκB pathways. Our data suggest that dual targeting of the PI3K-mTOR pathway disrupts both the catalytic and non-catalytic axes of EZH2 to inhibit metastasis and enhance cancer immune visibility, potentially increasing the utility of immunotherapy in resistant individuals.

INTRODUCTION

Breast cancer is the most common cancer in women worldwide (1). Triple-negative breast cancer (TNBC), which accounts for 15-20% of all breast cancers, is clinically challenging as it often recurs (2). TNBCs lack estrogen receptor, progesterone receptor, and human epidermal growth factor receptor 2 expression, limiting treatment options. Furthermore, TNBC is highly aggressive, with almost 50% of patients developing distant metastases to the brain, liver, and/or lung, at which point the median survival time is ~13 months (3). Responses to chemotherapy in patients with metastatic TNBC are often short-lived (4). While neoadjuvant immunochemotherapy has significantly improved the survival of patients with stage II–III TNBC (5,6), responses to immunotherapy are modest in metastatic settings and restricted to patients with high PD-L1 expression. Hence, there is an urgent need to develop new therapy regimens and targets for patients with TNBC, especially those that can be combined with immunotherapy.

Given its key role in tumorigenesis and immunity, targeting PI3K signaling has long been a therapeutic focus in cancer (7). However, pan-PI3K inhibitors are highly toxic, prompting the development of isoform-selective inhibitors (8), but results have been mixed. The PI3Kα inhibitor alpelisib (Piqray/NVP-BYL719; Novartis, Australia) combined with fulvestrant showed some efficacy in patients with metastatic breast cancer and after cyclin-dependent kinase 4 and 6 inhibitor (CDK4/6i) therapy, but with frequent adverse events and relatively short progression-free survival benefit (9). The dual PI3K-mTOR inhibitor paxalisib, which can cross the blood-brain barrier, has demonstrated promising clinical activity in glioblastoma (10-12) (NCT03522298, NCT03970447), solid tumor brain metastases (NCT03994796, NCT03765983, NCT04192981), DIPG/DMG (NCT03696355, NCT05009992), and primary CNS lymphoma (NCT04906096). Although individual mutations in individual PI3K pathway genes are relatively rare, when activating mutations in

PIK3CA and *AKT1* are combined with inactivating mutations in *PTEN*, the PI3K pathway is activated in 25–30% of advanced TNBCs (13). Therefore, revisiting PI3K pathway inhibition, especially in the immunotherapy era, is important to establish effective and safe combination regimens for patients with TNBC.

Here we demonstrate that dual targeting of the PI3K-mTOR pathway but not PI3K alone inhibits cancer cell proliferation and migration and promotes a mesenchymal-to-epithelial phenotype, simultaneously inhibiting signatures associated with metastasis-initiating cells (MICs), including the highly aggressive $CD44^{high}/CD24^{low}$ CSC phenotype, persister cancer cell phenotype (p65, FOXQ1, NRF2, NNMT), and drug resistance markers (ABCB5, SNAIL, ALDH1). *In vivo*, paxalisib overcomes immunotherapy resistance in TNBC to reduce primary tumor burden, circulating tumor cells (CTCs), and direct and indirect markers of metastasis with a favorable toxicity profile. Gene expression and spatial analyses show that paxalisib profoundly affects the tumor immune microenvironment, altering innate and adaptive inflammatory cell infiltrates into tumors, potentially through changes in IL-6 and induction of a viral mimicry gene signature. PI3K-mTOR blockade acts upstream of EZH2, impacting both the classical repressive catalytic p85β-EZH2-H27Me3 and active EZH2-NFκB pathways. Our data suggest that dual targeting of the PI3K-mTOR pathway disrupts both the catalytic and non-catalytic axes of EZH2 to exert both cell intrinsic and tumor immune microenvironment effects, potentially increasing the utility of immunotherapy in resistant individuals. Furthermore, as *PIK3R2*, which encodes p85β, was associated with prognostic and predictive outcomes, it may be a useful precision medicine biomarker for an at-risk group responsive to PI3K-mTOR inhibition.

METHODS

Cell culture

All cancer cell lines (4T1; RRID: CVCL_0125) mouse metastatic TNBC; MDA-MB-231 (RRID:CVCL_0062), MDA-MB-468 (RRID:CVCL_0419), SUM149PT (RRID:CVCL_3422) , human TNBC) were sourced from the ATCC (Gaithersburg, MD) and routinely mycoplasma tested using a MycoAlert^{TM} kit (Lonza). MDA-MB-231, MDA-MB-468 and SUM149PT lines were authenticated in-house by short-tandem repeat (STR) profiling using a GenePrint 10 kit (Promega). 4T1, MDA-MB-231, and SUM149PT cells were maintained and cultured in Dulbecco's Modified Eagle Medium (DMEM) (Gibco; Thermo Fisher Scientific, Waltham, MA; RRID: 11995073) supplemented with 10% FBS, 2 mM L-glutamine, and 1% penicillin/streptomycin (Gibco). MDA-MB-468 cells were maintained and cultured in Roswell Park Memorial Institute (RPMI) 1640 medium (Gibco) supplemented with 10% FBS, 2 mM L-glutamine, and 1% penicillin/streptomycin.

Inhibitors

For *in vitro* and *in vivo* studies, all PI3K and PI3K-mTOR pathway inhibitors (dactolisib, cat# S1009; apitolisib, cat# S2696; omipalisib, cat# S2658, LY294002, cat# S1105; alpelisib, cat# S2814; idelalisib, cat# S2226, and wortmannin, cat# s2758) were sourced from Selleck Chemicals LLC (Houston, TX). Paxalisib (GDC-0084; Kazia Therapeutics Ltd, NSW, Australia) was supplied under a materials transfer agreement. Chemical structures and International Union of Pure and Applied Chemistry (IUPAC) names of all PI3K inhibitors are detailed in Supplementary Table S1.

WST-1 cell viability assay

4T1, MDA-MB-231, MDA-MB-468, and SUM149PT cells were seeded at optimized densities in 96-well flat-bottom tissue culture plates in a total volume of 100 µl/well. Cells

were left to adhere overnight at 37°C and 5% CO_2 prior to treating with PI3K pathway inhibitors at the indicated doses. Cells were incubated at 37°C and 5% CO_2 for 72 hours, after which medium was removed and replaced with 100 µl/well of WST-1 cell proliferation reagent (Sigma-Aldrich) at a 1:10 final dilution in complete cell culture medium. Absorbance was recorded at 450 nm after a one-hour incubation period using a microplate spectrophotometer. Percent proliferation was calculated by subtracting the mean absorbance of the background control (blank) from the sample absorbance. The IC_{50} value of each inhibitor was determined by log(inhibitor) vs. response - variable slope using Prism 10 software (GraphPad Software, La Jolla, CA; RRID:SCR_002798).

Scratch wound healing assay

4T1 and MDA-MD-231 cells were stimulated with PMA/TGF-β as indicated above for 24 h prior to seeding at optimized cell densities in 96-well IncuCyte Image Lock plates (Sartorius, Göttingen, Germany). Cells were seeded in a total volume of 100 µl/well in low-serum medium (2%) and left to adhere overnight at 37°C and 5% CO_2 to ensure 100% confluency. After 24 h, wounds were created using the 96-pin IncuCyte WoundMaker Tool (Sartorius, Göttingen, Germany). Post wounding, cells were washed to remove non-adherent cells and then treated with PI3K pathway inhibitors in low-serum medium at the established IC_{50} doses. Plates were then placed into the IncuCyte Zoom live-cell analysis system (Sartorius, Göttingen, Germany), and wound healing was tracked using a scan interval of 4 hours over a 24-hour period. Samples were analyzed using IncuCyte ZOOM 2018A in-built analysis (Sartorius, Göttingen, Germany).

Flow cytometry

Fluorescence-activated cell sorting (FACS) was performed on single-cell suspensions stained with anti-CD44-BV650 (BioLegend Cat# 103049, RRID:AB_2562600) and anti-CD24-PE

antibodies (BD Biosciences Cat# 560991), with the LIVE/DEAD™ Fixable Aqua Dead Cell Stain Kit (Invitrogen; Thermo Fisher Scientific, Waltham. MA) to monitor cell viability. The proportion of $CD44^{high}/CD24^{low}$ cells were analyzed using Flow Jo software version 10.8.1 (BD Biosciences; RRID: SCR_008520) as described previously (14).

RNA extraction and cDNA synthesis

Cells were lysed in 500 µl TRIzol Reagent (Invitrogen; Thermo Fisher Scientific) before RNA isolation using the Direct-zol RNA Miniprep Kit (Zymo Research, Irvine, CA) and treated with RNase-free DNase I (Qiagen, Hilden, Germany) following the manufacturers' protocols. The NanoDrop (Thermo Fisher Scientific) instrument was then used to determine RNA concentration and purity (A260/A280). RNA (1 µg) was reverse transcribed to cDNA using the Superscript VILO IV Master Mix (Thermo Fisher Scientific) following the supplier's protocol. cDNA was diluted 1:20 with RNase-free water for qRT-PCR.

qRT-PCR

Gene transcription was analyzed using TaqMan Gene Expression Master Mix (Thermo Fisher Scientific) on the ABI Viia 7 real-time PCR machine (Applied Biosystems; Thermo Fisher Scientific). Cts were converted to arbitrary copy numbers and normalized to the geomean of the housekeeping genes *ACTB* and *PPIA*. The following human TaqMan probes were used: *ATR, ATM, RAD51, EXO1, IL6, GBP, IFIT1, IFIT2, IFIT3, IFIH1, IRF1, NFKB, RSAD2, P50, PDL1, PARP1*, *SNAI1*, *VIM,* and *EZH2*. No template and no reverse transcriptase controls were included to exclude genomic DNA contamination.

Human research ethics statement

The study was performed in accordance with the Declaration of Helsinki and informed consent was obtained in writing from all participants prior to study enrollment. This research was approved by the Metro North Human Research Ethics committee (Reference number

HREC/2020/QRBW/64831) and ACT Health Research Ethics Committee (Reference Number 2019.ETH.00080) and accepted by the QIMR Berghofer Medical Research Institute Human Research Ethics Committee under project numbers 3634 and 3659, respectively.

PBMC isolation

Whole blood from TNBC patients was stored in EDTA tubes for CTC identification. Unwanted cells were targeted using glycophorin A on red blood cells and then removed via centrifugation over a buoyant density medium (Lymphoprep™, STEMCELL Technologies, Vancouver, Canada). Purified PBMCs were then extracted as a highly enriched population from the interface between the plasma and the buoyant density medium and harvested in 20% FBS in PBS.

Circulating tumor cell enrichment

Whole blood from patients with TNBC was stored in EDTA tubes for CTC identification. RosetteSep™ Human CD45 Depletion Cocktail (STEMCELL Technologies) was used to enrich CTCs from whole blood by depleting $CD45^+$ cells. Unwanted cells were targeted for depletion with tetrameric antibody complexes recognizing CD45, CD66b, and glycophorin A on red blood cells. Unwanted cells were then removed via centrifugation over Lymphoprep™. The purified epithelial tumor cells were then extracted as a highly enriched population from the interface between the plasma and the buoyant density medium and were harvested in 20% FBS in PBS.

In the 4T1 intravenous (i.v.) metastasis mouse model, 300 µL of whole blood was collected from the submandibular vein and stored in EDTA tubes. ScreenCell®Cyto filtration devices (ScreenCell, Sarcelles, France) were used to capture single and clustered CTCs according to the manufacturer's instructions. Captured cells were validated as CTCs by immunofluorescence staining with primary antibodies targeting vimentin, Snail-1, and CD45.

Images were scanned using the Nikon Crest Optics Deep SIM super-resolution microscope (CrestOpics, Rome, Italy) and analyzed using ImageJ software (RRID:SCR_003070) as required.

Histochemistry and immunohistochemistry

The modified Giemsa staining methods is detailed in the **Supplementary Methods**. For human studies, immunohistochemistry was performed on five FFPE biopsy specimens from patients with stage III TNBC using an antibody directed against PIK3R2 (Atlas Antibodies Cat# HPA069291, RRID:AB_2686109) and imaged using the Aperio AT Turbo (Leica Biosystems). All tissues were analyzed for nuclear PIK3R2 (p85β) expression by a qualified pathologist and expressed as % positivity.

Immunofluorescence

MDA-MB-231 and MDA-MB-468 cells were cultured on glass microscope slides at optimized densities and fixed in 3.7% paraformaldehyde following treatment. CTCs and PBMCs were fixed in 3.7% paraformaldehyde, and cytospinning was used to mount them onto glass microscope slides. Cells were permeabilized by incubating with 0.5% Triton X 100 for 15 min, blocked with 1% BSA in PBS, and probed with primary antibodies as detailed in the **Supplementary Methods**. Protein expression was visualized with a donkey anti-rabbit Alexa Fluor 488, anti-mouse Alexa Fluor 568, or donkey anti-goat Alexa Fluor 647 (Thermo Fisher Scientific). Cover slips were mounted on glass microscope slides with ProLong Glass Antifade reagent (Thermo Fisher Scientific). Protein targets were imaged using the Zeiss 780 NLO confocal microscope (Zeiss, Oberkochen, Baden-Württemberg, Germany) or the Applied Spectral Imaging (ASI) Digital Pathology platform (Carlsbad, California) and analyzed using Imaris 10.1.1 (RRID:SCR_007370), QuPath (RRID:SCR_0182570), or automated ASI software, as required.

Duolink proximity ligation assay

MDA-MB-231 cells were seeded onto coverslips in 12-well plates at a density of 75,000 cells per well in 1 mL of growth medium (DMEM supplemented with 10% fetal bovine serum, 200 mM L-glutamine, and antibiotics) and incubated overnight at 37°C to allow for cell attachment. The following day, cells were treated with 10 µM paxalisib or DMSO (vehicle control) for 0.5, 2, 3, or 24 hours. Cells were then fixed with 3.7% formaldehyde and subjected to the Duolink proximity ligation assay (PLA; MilliporeSigma, Burlington, MA) according to the manufacturer's protocol. Briefly, cells were fixed and cytospinning was used to mount them onto glass microscope slides. PLA was performed using antibodies targeting p85β (Abcam Cat# ab16502, RRID:AB_443394) and H3K27Me3 (Abcam Cat# ab6002, RRID:AB_305237), p85β and EZH2 (Abcam Cat# ab283270, RRID:AB_3676493), and EZH2 and NFκB . Digital images were acquired on the Zeiss 780 NLO confocal microscope and analyzed using QuPath 0.4.3 software (RRID:SCR_018257).

Animal studies

The QIMR Berghofer Medical Research Institute Animal Ethics and Sai Life Sciences Institutional Animal Ethics committees approved all experimental procedures under study number A2109-627/Project ID 3761 and protocol number FB-24-112, respectively.

Six-to-eight-week-old female BALB/c mice were procured from the OzGene (Perth, Western Australia) and allowed to acclimatize for one week. For the orthotopic breast tumor model, 1 x 10^5 4T1 cells suspended in phosphate-buffered saline (PBS) were administered into the 4^{th} right mammary fat pad of BALB/c mice. For the i.v. metastatic breast cancer model, all female BALB/c mice were inoculated intravenously with 4T1 cells by tail vein injection with 0.1 mL of 1 x 10^5 cell suspension. In the murine colon adenocarcinoma “hot" tumor model (i.e., responsive to immunotherapy), 5×10^5 CT-26 cells were subcutaneously

implanted into the right flank of female BALB/c mice. Once primary tumors reached ~50-100 mm^3 or the day after IV inoculation, mice were subjected to daily oral administration of paxalisib at the indicated doses in combination with either anti-PD1 treatment (10 mg/kg) or anti-PD1+Abraxane (nab paclitaxel) (30 mg/kg) administered intraperitoneally at day 0 and day 4. Tumors were measured using calipers, and volumes were calculated using a modified ellipsoidal formula ½ (a/b^2), where a = longest side and b = shortest side. Mice were monitored daily for clinical abnormalities and tumor volumes were measured thrice weekly. Once tumors reached the maximum permitted size (1000 mm^3) in the vehicle group, all tumors and associated organs (lung, liver, spleen) were harvested, weighed, imaged, and fixed in 4% paraformaldehyde for subsequent analysis. For metastases studies, lungs were perfused with Indian ink and de-stained in Fekete's solution. Large protruding and small flat metastatic nodules were manually counted and the ratio of large:small quantified.

Tumor digestion

4T1 tumors were harvested in cold DMEM supplemented with 2.5% FCS before being finely cut using surgical scalpels and enzymatically dissociated using collagenase type 4 (Worthington Biochemical Corp., Lakewood, NJ) at a concentration of 1 mg collagenase/g of tumor at 37°C for 1 h. Dissociated cells were then passed through a 0.2 μm filter before fixation in 3.7% paraformaldehyde and cytospinning onto glass microscope slides for immunofluorescence staining.

NanoString nCounter assay

Total RNA was extracted from FFPE mouse tumor tissue using the RNeasy FFPE kit according to the manufacturer's protocols (Qiagen, Hilden, Germany). RNA concentration was measured using the Qubit RNA HS assay kit (Thermo Fisher Scientific).

RNA samples were subjected to hybridization with the multiplexed mouse tumor signaling 360 panel codeset. Then, hybridized samples were loaded onto nCounter prep station chips, and data were acquired using the nCounter Digital Analyzer (NanoString Technologies, Seattle, WA) following the manufacturer's procedures. Data were analyzed with nSolver Analysis Software v4.0 (NanoString Technologies). Counts were normalized according to the expression levels of housekeeping genes and positive/negative-control probes.

NanoString nCounter and RNA-seq/ChIP-seq integrated analysis

ChIP-Seq data (GSE223959) were accessed in scaled BigWig format for both MDA-MB-231 specific Input and EZH2 samples. BigWig files were converted to Wig format using bigWigToWig and further to bed format using wig2bed from the BEDOPS package (RRID:SCR_012865). EZH2 binding sites (peaks) of significant enrichment relative to input control were identified using MACS2 using the *callpeak* command by extending *in silico* the reads to a fragment size of 250 bp. Bound genes were defined as any ChIP-seq peak call that overlapped a gene body +/-3 kb; bound promoters were defined as any ChIP-seq peak call that overlapped a transcription start site (TSS) +/-3 kb. ChIP-Seq peaks were annotated using ChIPseeker R package (RRID:SCR_021322).

EZH2 chromatin-binding sites in MDA-MB-231 cells were compared to publicly available MDA-MB-231 ChIP-seq data of the repressive mark H3K27me3 (GSE77772) obtained in BigWig format containing the log-transformed fold-enriched in ChIP relative to Input. bigWigToBedGraph was used to convert to BedGraph format, which was further used for calling peaks (binding sites) using MACS2 bdgpeakcall with a cut-off of 0.5. Further, nCounter Tumor 360 Signaling panel genes bound by EZH2 were checked for overlap with genes bound by H3K27me3.

STEP spatial immune profiling and analysis

OCT frozen mouse tumor tissues were immunolabelled with an 18-panel antibody cocktail (CD19, CD21/35, CD3, TCRb, CD4, CD90.2, CD11b, CD45, Ly6G, IgM, CD24, CD11c, CD38, CD31, Ter119, CD49f, CD71, Ki67) and subjected to the Spatial Tissue Exploration Program (STEP) platform (Akoya Biosciences, Marlborough, MA).

Multiplexed Image Bioinformatics analysis

Data preprocessing

The final QPTIFF files of composite images were opened in QuPath (15), where quality control can be performed by visual assessment of the whole slide. All markers were evaluated individually based on appropriate cellular localization and staining pattern. Artifacts such as debris, tissue folding, and out-of-focus regions were manually cropped and excluded from the downstream analysis.

Segmentation and phenotyping

Nuclear segmentation was first performed using StarDist to the DAPI channel, with the deep learning model retrained by Akoya internally (16). Cytoplasm segmentation was then estimated from nuclear expansion by morphological dilation of 6 μm. The centroid of each cell was determined by the x-y coordinates within the image. Mean fluorescent intensity (MFI) of each marker was extracted for each segmented cell from the nuclear mask and cytoplasm mask according to protein localization, yielding a single-cell protein signals matrix. Cells without any marker expression or abnormally high signal sum were removed. Cell segmentation and filtering left 528,659 cells across two samples.

Each protein signal was then z-scored across all cells, such that each marker had a mean of zero and a standard deviation of one. Only QC-passed lineage markers were used for

phenotyping analysis. The Leiden algorithm and GPU-accelerated methods were used for unsupervised clustering, with cluster visualization using UMAP and t-SNE (17,18). For Leiden clusters, resolutions of 1-6 were tested, and the optimal resolution of 2 was chosen for subclustering and manual annotation. We performed multi-level refinement by additional rounds of subclustering of unclear clusters. Clusters were visualized and annotated on the image after each clustering. Cell phenotypes were assigned based on protein expression in the hierarchical clustering heatmaps and their location in the images. Clusters with similar expression patterns were combined. The number of cell types was then calculated, and the percentages were compared across different samples.

Cellular neighborhood analysis

Cellular neighborhood (CN) analysis was performed as previously described (19). Briefly, for each annotated cell, we use the *k*-nearest neighbor algorithm to enumerate the cell types of its 10 nearest spatial neighbors (including the center cell) in Euclidean space. These local neighborhood windows were then clustered based on the composition of cell types within each window using the MiniBatchKMeans algorithm, with k=10. Each cell was then allocated to the CN defined by the containing window. CNs were annotated based on the enrichment of certain cell types. The percentage of each CN was also calculated.

Population-based cancer survival analysis

Human cancer datasets meeting the following criteria were downloaded from Array Express (AE), Gene Expression Omnibus (GEO; RRID:SCR_005012), and Sequence Read Archive (SRA; RRID:SCR_004891): (a) at least 20 expression profiles from cancer patient tissues (not cell lines or preclinical models); (b) annotated with clinical outcomes of at least one of i) categorical outcomes after treatment, e.g., progressive disease, stable disease, pathological complete response, response, no response, and distant metastasis; and/or ii) continuous

outcome data including survival and event follow-up, e.g., overall, disease-specific, distant metastasis-free, or progression-free survival.

For cohort analysis, within each cohort, we compared the mRNA expression levels of *PIK3R2* by categorizing the samples into high- and low-risk subgroups, e.g., high risk = distant metastasis and low risk = no metastasis. Samples were also categorized into high and low subgroups based on *PIK3R2* expression, where high = ≥75th percentile of *PIK3R2* expression and low = <75th percentile. Where mutation or copy-number data were available, samples were categorized into altered and unaltered for the *PIK3R2* gene: altered = harbors a mutation or copy number change in *PIK3R2*; unaltered = otherwise. Box and scatter plots comparing *PIK3R2* expression between the above subgroups were plotted using the ggplot package in R version>4.0 (20). Statistical significance between subgroups was compared with the Wilcoxon test. Kaplan-Meier survival curves between high- and low-risk groups were plotted using the ggsurve package and the statistical difference between the curves were computed using log-rank test.

Statistical analysis

Statistical significance was assessed in Prism 10 (GraphPad Software, La Jolla, CA) using either paired or unpaired *t*-tests or one-way ANOVA (Dunnett's or Tukey's multiple comparison test), as indicated. $P \leq 0.05$ was considered statistically significant (*, $P < 0.05$; **, $P < 0.01$; ***, $P < 0.001$; ****, $P < 0.0001$).

Data availability

All data are available upon reasonable request.

RESULTS

Dual PI3K-mTOR blockade with paxalisib inhibits proliferation and migration, induces mesenchymal to epithelial transition, and reduces MIC signatures

We first compared the efficacy of pan-PI3K, isoform-specific PI3K, and dual targeting PI3K-mTOR inhibition in MDA-MB-231, MDA-MB-468, SUM149PT, and 4T1 cells (a mouse line with a "cold" tumor profile, i.e., unresponsive to immunotherapy) using wortmannin (pan-PI3K inhibitor), idelalisib (p110 δ,γ inhibitor), alpelisib (p110α inhibitor), and LY294002 (p110α,β,δ inhibitor) and the dual PI3K-mTOR inhibitors omipalisib (p110α/β/δ/γ,mTORC1/2), apitolisib (PI3Kα/β/δ/γ, mTOR), dactolisib (p110α,β,δ,γ, mTOR), and paxalisib (p110α,β,δ,γ, mTOR inhibitor) (**Figure 1A, Supplementary Figure 1A and Supplementary Table S1**). The inhibitory effect of dual PI3K-mTOR inhibitors was greater than that of pan- or isoform-specific inhibitors in MDA-MB-231 TNBC cells, with paxalisib, omipalisib, apitolisib, and dactolisib all having IC_{50} values ≤2.5 μM (**Figure 1A**). Dual PI3K-mTOR inhibition with paxalisib and dactolisib was similarly effective in MDA-MB-468 and SUM149PT TNBC cells, and paxalisib had an IC_{50} of 0.33 μM in 4T1 cells (**Supplementary Figure 1A**). Furthermore, PI3K/PI3K-mTOR inhibition with paxalisib inhibited cancer cell migration in the MDA-MB-231(**Figure 1B**) and 4T1 (**Supplementary Figure 1B**) models. Given the favorable *in vitro* inhibitory profile of paxalisib, we used this inhibitor in subsequent experiments.

Several cancer cell populations, including cancer stem cells (CSCs), dormant tumor cells, and persister cancer cells, referred to here as metastasis-initiating cells (MICs), are implicated in metastases and drug resistance (21). Given that PI3K/mTOR signaling is strongly implicated in TNBC tropism, EMT, and stemness (22,23), we next examined the effects of paxalisib on EMT and MIC characteristics in cancer cells *in vitro*. In MDA-MB-231 TNBC cells, paxalisib treatment reduced expression of the mesenchymal marker

vimentin and increased protein expression of the epithelial marker E-cadherin (**Figure 1C,D**). Furthermore, we determined the impact of paxalisib on the $CD44^{high}/CD24^{low}$ population, which is associated with the EMT and CSC trait (24), and PI3K-mTOR inhibition reduced the CD44/CD24 ratio by 67% in MDA-MB-231 cells (**Figure 1E**). Paxalisib also reduced protein expression of three biomarkers associated with drug resistance and the CSC phenotype (25), ABCB5, ALDH1, and Snail (**Figure 1F**) and markers associated with persister cancer cells, NFκB p65, FOXQ1, NNMT, and NRF2 (**Figure 1G**). To ensure convergence between human *in vitro* findings and subsequent *in vivo* studies in mice, we quantified changes in expression of CSC (*VIM*), resistance (*SNAI1*), and persister cell (*NFKB, FOXQ1*) markers in 4T1 TNBCs from mice treated with or without paxalisib, which showed similar decreases in expression after paxalisib treatment (**Supplementary Figure 1C**). Taken together, these data indicate that PI3K-mTOR blockade reverses the dynamic EMT process and induces a mesenchymal-to-epithelial phenotype less associated with the hallmarks of MICs.

Given the importance of inflammation in driving metastases, we next determined the role of the PI3K-mTOR inhibition on pro-inflammatory cytokine production and cancer immune visibility. Treatment of CTCs isolated from TNBC patients with paxalisib reduced IL-6 protein expression by 72% in $ABCB5^{+}EpCAM^{+}$ CTCs (**Figure 1H**). Finally, induction of a viral mimicry gene signature has been shown to re-invigorate adaptive immune responses, thereby improving responses to immunotherapy (26). To further investigate this signature in TNBC cells, MDA-MB-231 cells were treated with paxalisib for 24 h (**Figure 1I**). Exposure to paxalisib significantly increased expression of several viral mimicry genes, most profoundly GBP2 (**Figure 1I**). Changes in mRNA expression only occurred in response to PI3K-mTOR inhibition (paxalisib and dactolisib; **Figure 1J**), further supporting the importance of dual PI3K-mTOR inhibition for the induction of cancer immune visibility.

Paxalisib reduces primary tumor burden and metastasis with a favorable toxicity profile

We next sought to test the efficacy of paxalisib in a clinically-relevant model of immunotherapy resistance in TNBC, the spontaneous metastasis 4T1 TNBC model (**Figure 2A**). As paxalisib alone (and anti-PD1, as expected) did not reduce primary tumor volume (**Figure 2B**), paxalisib was combined with anti-PD1 and, in a split-dose de-escalation study (**Supplementary Figure 2A**), 7.5 mg/kg was confirmed as the optimal dose for maximum efficacy (**Supplementary Figure 2B**) with minimal toxicity when compared with higher doses, as measured by body and liver weights (**Supplementary Figure 2C,D and Supplementary Results**). Consistent with liver weight data, the optimal therapeutic dose of 7.5 mg/kg was not hepatotoxic as assessed by histopathological examination, compared with higher doses (**Figure 2C, left**). As the addition of immunotherapy to neoadjuvant chemotherapy has significantly improved outcomes for patients with stage II–III TNBC and patients with metastatic TNBC expressing high levels of PD-L1 (5,6), but some patients experience drug resistance, we also administered paxalisib in combination with immunotherapy (anti-PD1) +/- chemotherapy (Abraxane) in the 4T1 model (**Figure 2B, Supplementary Figure 2E,F**). The triple combination of paxalisib + anti-PD1 + Abraxane showed the greatest reductions in primary tumor weight and volume (**Figure 2B**), with no increase in toxicity (**Supplementary Figure 2E,F**).

In the 4T1 model, 4T1 mouse breast tumor cells are injected into the mammary gland of host mice and metastases usually then develop in the lung, lymph nodes, liver, bone and other sites. However, mice treated with the paxalisib-anti-PD1 combination regimen did not develop overt metastasis, suggesting an anti-metastatic effect. Lung inflammatory infiltrates, enlarged spleens (splenomegaly), and extramedullary hematopoiesis (EMH) are associated with cancer progression and metastasis in the 4T1 model even in the absence of macroscopic

disease (27). Supporting a systemic anti-cancer effect of combined paxalisib-anti-PD1, histopathological examination of the lungs revealed a significant decrease in leukocyte infiltration into the lungs at all concentrations, including at the optimal therapeutic dose of 7.5 mg/kg (**Figure 2C, middle**), and there was a significant reduction in EMH following paxalisib treatment at the optimal therapeutic dose of 7.5 mg/kg (**Figure 2C, right**).

To further assess the impact of paxalisib on tumor metastasis, we injected 4T1 tumor cells into the systemic circulation prior to treatment (**Figure 2D**). Mice treated with paxalisib combined with anti-PD1 maintained normal body weights throughout the first 10 days of the experiment (**Figure 2E**). $CD45^{-}VIM^{+}SNAIL^{+}$ CTCs (**Figure 2F**) were isolated from whole blood collected from the submandibular vein using the ScreenCell®Cyto filtration device. Significantly fewer CTCs (<300 cells) were captured from paxalisib + anti-PD1-treated mice compared with vehicle mice (>1500 cells) (**Figure 2G,H**). We also inflated lungs with Indian ink to visualize metastatic lung nodules (**Figure 2I**), and systematic examination revealed two metastatic phenotypes: large and protruding or small and flat (**Figure 2I**). There was a significant reduction in the number of both types of metastases when mice were administered paxalisib and anti-PD1 (**Figure 2I**). Therefore, paxalisib inhibits CTCs and the development of metastases.

Spatial imaging reveals changes in immune cell landscapes when paxalisib is combined with immunotherapy

To examine the effects of paxalisib on the tissue microenvironment, we next used spatial immune profiling of tumor tissues from the 4T1 TNBC model to investigate 14 innate and adaptive immune populations, stromal cells, and tumor cell proliferation and their interactions following treatment with paxalisib combined with immunotherapy using a 23-marker (immuno)phenotyping panel (**Figure 3A, Supplementary Table S2**). The addition of

paxalisib to anti-PD1 treatment reduced the proportion of stromal cells (mainly vascular cells, but also fibroblasts and erythrocytes) (**Figure 3B**), increased adaptive immune cell populations, particularly B cells (**Figure 3B**), and increased specific populations of innate immune cells (like neutrophils and dendritic cells), while decreasing others (like macrophages) (**Figure 3B**). The patterns of infiltration also differed between treatment groups, with B cells and neutrophils accumulating in the center of the tumors and others, like APCs and macrophages, observed at the periphery (**Figure 3C**).

To explore potential interactions between immune cell populations, we conducted cellular neighborhood (CN) analysis (**Figure 3D**). CN analysis identified ten unique cellular neighborhoods, with an increase in B cell and neutrophil populations in the center of paxalisib + anti-PD1 tumors and DCs at the periphery, and a decrease in macrophages (central) and stromal cells (throughout) (**Figure 3E**). Paxalisib has a profound effect on the tumor microenvironment, affecting both the immune and stromal compartments.

PI3K-mTOR inhibition enhances anti-tumor immune profiles in combination with immunotherapy

To further understand immune cell changes in the microenvironment of paxalisib-treated tumors at higher resolution, we conducted NanoString nCounter analysis of tumors harvested from the 4T1 model. Paxalisib + anti-PD1 treatment enhanced anti-tumor immune responses in both paxalisib and combination treatments, such as increases in antigen presentation, TCR signaling, cytotoxicity, and interferon responses (**Supplementary Figure 3**). Cell abundance analysis revealed increases in anti-tumor immune cell populations in response to paxalisib and paxalisib + anti-PD1 treatment, including in cytotoxic cells, dendritic cells (DCs), T cells, and B cells (**Figure 4A**). Supporting a more favorable therapeutic outcome, relative cell abundance analysis also revealed increased total tumor-infiltrating lymphocyte (TIL) counts

in both paxalisib and combination treatment groups, representing a shift in lymphocyte populations through an increase in B cells, mirroring the spatial analysis and notable decreases in exhausted and regulatory T cell populations, providing a more granular analysis of the subtype distribution (**Figure 4B**). Importantly, cytotoxic T cell function was also increased in response to paxalisib, with increases in granzyme B (Gzmb) and IFNγ expression (**Figure 4C**). Paxalisib and combination therapies also inhibited pro-tumor immune cell populations such as mast cells, which contribute to anti-PD1 resistance and immune-suppressive regulatory T cells (**Figure 4D**). Mast cell differences were further confirmed at the tissue level using toluidine blue (**Figure 4E**).

Collectively, these findings demonstrate that paxalisib + anti-PD1 treatment induces anti-tumor immune profiles (cytotoxic T cells), reduces T cell phenotypes associated with immunotherapy resistance (exhausted T cells, Tregs), whilst reducing pro-tumor innate immune populations such as mast cells.

PI3K-mTOR inhibition targets p85β-H3K27Me3 interactions

Recent studies have shown that p85 regulatory subunit of PI3K can regulate biological processes through nuclear translocation (28). Nuclear translocation of p85β stabilizes EZH1/2, increasing H3K27 tri-methylation and gene silencing (28). Therefore, we sought to confirm nuclear p85β expression in human TNBC. Immunohistochemistry was performed on cancer tissues from stage 3 TNBC patients (**Supplementary Figure 4**), and sections were analyzed by an independent histopathologist blinded to the treatment groups. Consistent numbers of nuclear $p85\beta^{+}$ cells were observed in all patient tissues, thereby confirming nuclear p85β expression in TNBC (**Supplementary Figure 4**). This pattern of expression was also confirmed *in vivo* in mouse tumor cells isolated from mice treated with combined paxalisib, chemotherapy, and/or immunotherapy (**Supplementary Figure 5A,B**). Reduced

nuclear p85β expression was observed in paxalisib and paxalisib + anti-PD1-treated mice, suggesting a direct impact of PI3K-mTOR inhibition on the translocation of p85β into the nucleus (**Supplementary Figure 5B**).

Given p85β nuclear translocation leads to increased H3K27 tri-methylation, we next determined the impact of paxalisib treatment on p85β and H3K27Me3 nuclear expression. Paxalisib alone or triple combination-treated 4T1 mice showed a significant decrease in both nuclear p85β and H3K27me3 expression in vimentin^{+} cells (**Supplementary Figure 5C**). Immunofluorescence analysis revealed a significant decrease in the nuclear intensity of p85β and H3K27Me3 (**Figure 5A**) in response to paxalisib in MDA-MB-231 and MDA-MB-468 cells (**Figure 5B**). Notably, co-localization of p85β and H3K27Me3 was observed in vehicle but not paxalisib-treated samples (**Figure 5A**). Finally, to determine the relevance of this p85β:H3K27Me3 interaction in TNBC patients, PBMCs were isolated from the blood of TNBC patients before and after chemotherapy and subjected to Duolink PLA (**Supplementary Figure 5D**). Elevated nuclear p85β:H3K27Me3 interactions were observed after chemotherapy in all patients (**Supplementary Figure 5E**), suggesting an association with drug resistance.

PI3K-mTOR inhibition targets the dual role of EZH2

EZH2 has been implicated in metastases and recurrence via two mechanisms (29). First, EZH2 catalyzes H3K27 tri-methylation (30,31), acting as a transcriptional repressor and causing epigenetic gene silencing (30-32). Second, EZH2 has a non-catalytic inducible role as a transcriptional co-activator, interacting with NF-κB p65, resulting in the positive regulation of cancer-related (EMT, cell cycle, DNA repair) and NF-κB inflammatory target genes (30).

To investigate the impact of PI3K-mTOR inhibition on EZH2 expression, MDA-MB-231 cells were treated with paxalisib for 24 h prior to immunofluorescence and qPCR analysis. PI3K-mTOR blockade reduced EZH2 mRNA (**Figure 6A**) and corresponding protein levels within the nucleus (**Figure 6B**). Furthermore, paxalisib significantly decreased nuclear p85β:EZH2 (**Figure 6C**) and p65NFκB:EZH2 (**Figure 6D**) interactions, as observed by proximity ligation assays. Time course analysis quantifying the interaction between p85β and EZH2 showed decreased interactions immediately after addition of the inhibitor at 30 minutes, 2 hours, and 3 hours post-paxalisib treatment in MDA-MB-231 cells (**Supplementary Figure 5F**), suggesting an immediate impact of the drug on existing p85β:EZH2 interactions even prior to changes in transcript levels of EZH2 (**Supplementary Figure 5G**) (33).

To investigate the impact of paxalisib on EZH2-targeted gene expression, we overlapped EZH2/H3K27me3 ChIP-seq data (30) with our NanoString nCounter differentially-expressed (DE) genes (**Figure 6E**). EZH2-bound genes ($EZH2^+$) were mainly upregulated by paxalisib (30 DE genes) and paxalisib + anti-PD1 (19 DE genes) treatments, while anti-PD1 alone mediated nine DE genes with EZH2-binding sites. Notably, there were no common $EZH2^+$ DE genes between paxalisib and anti-PD1 treatments, indicating that they have an impact on completely different biological pathways. We further employed H3K27me3 ChIP-seq data to distinguish the chromatin states of EZH2-bound DE genes, showing that half of the $EZH2^+$ population was associated with the repressive mark H3K27me3 ($EZH2^+/K27me3^+$). We next determined the distribution of EZH2-bound genomic locations of both up- and downregulated DE genes after paxalisib and anti-PD1 treatment (**Figure 6F**). There were distinct EZH2-binding patterns between up- and downregulated genes after paxalisib and anti-PD1 treatment. EZH2 mainly bound at distal intergenic (40%) and promoter (TSS +/- 2-3 kb, 5.9%) regions of upregulated genes, while

more proximal promoter regions (TSS ≤ 1 kb, 37.2%; and TSS +/- 1-2 kb, 9.3%) were bound by EZH2.

A recent study revealed that EZH2 co-localizes with NF-κB to activate pro-oncogenic gene expression in TNBC (30). Consistently, we found that genes associated with inflammation (IL-6), the drug-resistant phenotype (FOXQ1, NNMT, RelA, NFE2L2), and TNBC metastasis (KRT14) were all bound by both EZH2 and NFκB2 in MDA-MB-231 cells (**Figure 6G and Supplementary Figure 6**).

Together, paxalisib and anti-PD1-mediated $EZH2^{+}/K27me3^{+}$ genes are potential gene signatures and therapeutic targets in recurrent cancer. Interestingly, three $EZH2^{+}/K27me3^{+}$ genes were also co-occupied by NFκB2, suggesting that $EZH2^{+}/K27me3^{+}/NF\kappa B2^{+}$ may function as repressor complex in TNBC, since NF-κB both activates and represses gene expression (34).

Associations between PIK3R2 gene expression and survival in patients with TNBC

Finally, we analyzed whether expression of *PIK3R2*, which encodes p85β, was associated with outcomes in TNBC/basal-like breast cancer (GSE158309 dataset (20)). Patients with basal-like/TNBC expressing high levels of *PIK3R2* (solid lines) showed poorer distant metastasis-free survival (DMFS) than patients with low expression (**Supplementary Figure 7A**).

Next, we assessed *PIK3R2* mRNA expression in stage IV metastatic TNBC post chemotherapy (carboplatin, nab-paclitaxel) + pembrolizumab durvalumab + olaparib in a single-arm phase-2 trial (35) (**Supplementary Figure 7B**). Patients with higher mRNA expression of *PIK3R2* showed poorer overall survival compared with patients with lower *PIK3R2* mRNA expression. In addition, higher pre-treatment levels of *PIK3R2* were positively associated with distant relapse in TNBC patients who had residual tumors after

treatment with neoadjuvant chemotherapy (NACT) (36) (**Supplementary Figure 7C)**. PIK3R2 could be a useful prognostic and predictive biomarker.

DISCUSSION

Here we provide novel insights into the contribution of the PI3K-mTOR pathway to the TNBC phenotypes associated with growth, migration, metastasis, and therapy resistance. Specifically, we demonstrate that dual targeting of PI3K and mTOR but not PI3K alone inhibits cancer cell proliferation and migration *in vitro*. Using paxalisib to probe dual PI3K-mTOR pathway inhibition, we find that it not only promotes a favorable mesenchymal to epithelial phenotype but also inhibits signatures associated with MICs, including CSC, persister cancer cell, and drug resistance signatures. *In vivo*, paxalisib overcomes immunotherapy resistance to reduce primary tumor burden, circulating CTCs, and metastasis with a favorable toxicity profile. Paxalisib also profoundly affects the tumor immune microenvironment, reducing adaptive immune phenotypes associated with immunotherapy resistance (exhausted T cells, Tregs) and pro-tumor innate immune populations such as mast cells. PI3K-mTOR blockade acts upstream of EZH2, impacting both the classical repressive catalytic p85β-EZH2-H27Me3 and active EZH2-NFκB pathways. Our data suggest that dual targeting of the PI3K-mTOR pathway disrupts both the catalytic and non-catalytic actions of EZH2 to inhibit metastasis and promote an immunogenic tumor immune microenvironment that could increase the utility of immunotherapy in resistant individuals. Furthermore, expression of *PIK3R2*, which encodes p85β, was associated with poor prognostic and predictive outcomes in patients with TNBC, paving the way for a precision medicine biomarker for an at-risk group that might be most responsive to PI3K-mTOR inhibition.

These experiments highlight the importance of dual targeting not only PI3K but also mTOR in tumor cells to reduce or prevent metastases and create a pro-immunogenic tumor immune microenvironment (**Figure 7, Mechanism 1**). MICs are implicated in metastases and are enriched following standard-of-care treatments (21). CSCs, which express high levels of ABCB5, ALDH1, CD44, and EpCAM, are defined by their tumor re-populating ability, drug resistance, plasticity, and metastatic capacity (37). Dormant tumor cells, which may remain quiescent for a long time, are found in naïve tumors, drug-treated tumors, and pre-metastatic sites. These cells are characterized by slow proliferation and increased expression of stemness, EMT, plasticity, and drug-resistance markers (37). Persister cancer cells surviving drug treatment (38) are highly plastic cells that express genes associated with EMT (*TAGLN* and *NNMT*), stemness, and the tumor-necrosis factor-α (TNF-α)-nuclear factor κB (NF-κB) inflammatory pathway (38-40). Originating from mutations or epigenetic reprogramming (41), collectively, MICs contribute to metastases and recurrence. Using paxalisib as an exemplar PI3K/mTOR inhibitor, we show that this pathway is critical for targeting metastatic processes. Specifically demonstrate that paxalisib: i) inhibits the CSC phenotype ($CD44^{high}$ $CD24^{low}$) in human TNBC cells; ii) simultaneously inhibits protein and mRNA expression of MIC-related genes and the IL-6 and NFκB inflammation signature whilst inducing viral mimicry programs *in vitro*; and iii) targets CTCs in the blood and significantly inhibits the growth of lung metastases when combined with anti-PD1. As a major mediator of the immune response, high levels of IL-6 are associated with a poor prognosis, drug resistance, and metastases (42-44). Together with inhibiting MIC signatures and inflammation, we show that our approach also induces immune re-invigoration and cancer immune visibility (**Figure 7, Mechanism 1**). Epigenetic therapies that activate viral mimicry may enhance adaptive immune responses by increasing antigen processing and presentation, resulting in increased tumor immunogenicity, T cell infiltration, and enhanced immunotherapy responses (29,45).

Our spatial and transcriptomic analyses support that paxalisib may promote these mechanisms, as immunotherapy-resistant tumors showed a reduction in adaptive immune phenotypes associated with immunotherapy resistance (exhausted T cells, Tregs) and pro-tumor innate immune populations such as mast cells after treatment with paxalisib.

We show that the nuclear p85β subunit is enriched in TNBC human cell lines and after chemo and immunotherapy so might be a marker of residual disease. There is accumulating evidence that EZH2 is a key factor controlling drug resistance via its dual functionality (46). A component of polycomb repressive complex 2 (PRC2), EZH2 is overexpressed in many solid cancers and has been associated with cancer progression and poor survival outcomes (30,47-51). EZH2 catalyzes the tri-methylation of lysine 27 on histone H3 (H3K27me3) (30,31), acting as a transcriptional repressor and epigenetic gene silencer (30-32). Recent studies have also identified a non-catalytic role for EZH2 independent of H3K27Me3 as a transcriptional co-activator (30,32,52). EZH2 physically interacts with NF-κB p65 (RelA) in TNBC cells, independent of PRC2, resulting in the positive regulation of cancer-related (EMT, cell cycle, DNA repair) and NF-κB target genes, including the pro-inflammatory cytokine IL-6 (30). These two functions of EZH2 modulate critical signaling pathways that cause drug resistance. Current drugs that solely target the canonical catalytic activity of EZH2 result in incomplete responses or primary resistance (53,54). Given that NF-κB signaling also participates in resistance (55,56), identifying therapeutic strategies that target both the catalytic and non-catalytic roles of EZH2 might better overcome resistance mechanisms, consequently improving clinical outcomes (**Figure 7, Mechanism 2**). Our results show that nuclear p85β colocalizes with EZH2 in an epigenetic complex. Paxalisib disrupts the nuclear p85β-EZH2 complex in human TNBC cells and patient-derived TNBC liquid biopsies treated *ex vivo*. EZH2 also interacts with the PI3K/Akt)/mTOR pathway (28,46). Existing as a heterodimer, PI3K consists of a p110

catalytic subunit (p110α, p110β, and p110δ) and a p85 repressive regulatory subunit (p85α, p85β, p55α, p50α, and p55γ) (57). p85 proteins can regulate biological processes through nuclear translocation (28). Specifically, p85β disassociates from p110α in cancer cells, translocating to the nucleus, stabilizing EZH1/2, and increasing H3K27 tri-methylation (28). Thus, our findings highlight for the first time that PI3K-mTOR inhibition disrupts both the established p110-p85α complex (**Supplementary Table S3**) and the nuclear p85β-EZH2 complex. Thus, PI3K-mTOR inhibitors disrupt both the cytoplasmic and nuclear PI3K axes, which is critical for suppressing the complete contribution of the PI3K pathway in cancer. The precise mechanism of action needs further study. Nevertheless, our findings show that paxalisib inhibits EZH2 transcription, contributing to the overall disruption of the nuclear EZH2 pool. Future studies exploring the contribution of mTOR or p85β to regulating the promoter of EZH2 will be required.

More recently, a non-catalytic role for EZH2 has been identified, in which it acts as a transcriptional co-activator (30,32,52). In the context of TNBC, EZH2 interacts with NF-κB p65, inducing EMT and NF-κB inflammatory target genes (30). To date, EZH2 inhibitors have underperformed clinically, with partial responses or primary resistance major limitations (53,54). We now extend recent findings by demonstrating the importance of targeting signaling pathways upstream of EZH2. By inhibiting the PI3K-mTOR pathway through p85β nuclear translocation, we targeted both the catalytic and non-catalytic axes of EZH2, thereby overcoming resistance mechanisms and reducing metastases (**Figure 7, Mechanism 2**). Future studies are needed to evaluate the precise mechanism(s) by which the PI3K-mTOR pathway inhibits both axes of downstream EZH2. Nevertheless, this study provides critical evidence for the use of PI3K-mTOR inhibitors such as paxalisib in the treatment of TNBC.

In conclusion, this study demonstrates the utility of combining PI3K-mTOR inhibitors with immunotherapy by exploiting interactions between the PI3K-mTOR signaling pathway and the EZH2 epigenetic network. For the first time we show that dual targeting of the PI3K-mTOR pathway, not PI3K alone, has beneficial effects by inhibiting signatures associated with MICs, altering the tumor immune microenvironment, preventing metastases, and overcoming resistance associated with immunotherapy. These results pave the way for further testing of PI3K/mTOR inhibitors with immunotherapy in TNBC.

AUTHOR CONTRIBUTIONS

M. Melino: Conceptualization, methodology, data curation, formal analysis, supervision, writing-original draft, writing-review and editing. **W. Tu**: Conceptualization, Methodology, data curation, formal analysis, supervision, writing and re-structuring the manuscript, writing-review and editing. **H. Bielefeldt-Ohmann**: Pathology assessment, data curation, and analysis. **M. Proctor**: Methodology, data curation and analysis. **T. Ahuja**: Methodology, data curation and analysis. **J. Vandermeide**: Methodology, data curation and analysis. **A.Bain**: Ethics writing, study design and submission, human research sample co-ordination. **G. Nallan**: Methodology, data curation. **S. Goh**: Methodology, data curation. **T. Prassana**: Methodology, data curation, analysis, clinical support. **J. Dahlstrom**: Pathology advisory support. **M. Miranda**: Methodology, data curation. **R. Choudhary, A. Anandam, S. Chaudhary, J. Seal**: Methodology, data curation. **D. Sinha**: Methodology. **S. Zhang**: Data analysis. **T. Nguyen**: Data analysis. **S. Srihari**: Data analysis. **G. Hartel**: Statistical support. **A. Ives**: Trial co-ordinator. **L. Malik**, **D. Yip**, **M. Nottage**, **M. Eastgate**: Clinician advisory support. **S. Rao**: Overall study lead, conceptualization, resources, formal analysis, supervision, funding acquisition, visualization, writing–review and editing.

ACKNOWLEDGEMENTS

S. Rao is supported by an Inaugural Daniela Dwyer foundation fellowship. Funding was provided by collaborative agreement between Kazia Therapeutics Limited and QIMR Berghofer Medical Research Institute. We would like to thank Dr. Jenny Dunn for technical assistance with wound healing assays and the Scientific Services team at QIMR Berghofer Medical Research Institute for their support with animal handling, histology, and imaging. Finally, we are grateful to the patients, clinicians, and pathologists who contributed patient material to this study.

REFERENCES

1. Bray F, Laversanne M, Sung H, Ferlay J, Siegel RL, Soerjomataram I, *et al.* Global cancer statistics 2022: GLOBOCAN estimates of incidence and mortality worldwide for 36 cancers in 185 countries. *CA: A Cancer Journal for Clinicians* 2024;**74**(3):229-63 doi https://doi.org/10.3322/caac.21834.
2. Yin L, Duan JJ, Bian XW, Yu SC. Triple-negative breast cancer molecular subtyping and treatment progress. *Breast Cancer Res* 2020;**22**(1):61 doi 10.1186/s13058-020-01296-5.
3. Kesireddy M, Elsayed L, Shostrom VK, Agarwal P, Asif S, Yellala A, *et al.* Overall Survival and Prognostic Factors in Metastatic Triple-Negative Breast Cancer: A National Cancer Database Analysis. *Cancers* 2024;**16**(10):1791.
4. Huppert LA, Gumusay O, Rugo HS. Emerging treatment strategies for metastatic triple-negative breast cancer. *Ther Adv Med Oncol* 2022;**14**:17588359221086916 doi 10.1177/17588359221086916.
5. Tarantino P, Corti C, Schmid P, Cortes J, Mittendorf EA, Rugo H, *et al.* Immunotherapy for early triple negative breast cancer: research agenda for the next decade. *NPJ Breast Cancer* 2022;**8**(1):23 doi 10.1038/s41523-022-00386-1.
6. Cortes J, Rugo HS, Cescon DW, Im S-A, Yusof MM, Gallardo C, *et al.* Pembrolizumab plus Chemotherapy in Advanced Triple-Negative Breast Cancer. *New England Journal of Medicine* 2022;**387**(3):217-26 doi doi:10.1056/NEJMoa2202809.
7. Vanhaesebroeck B, Perry MWD, Brown JR, Andre F, Okkenhaug K. PI3K inhibitors are finally coming of age. *Nat Rev Drug Discov* 2021;**20**(10):741-69 doi 10.1038/s41573-021-00209-1.

8. Sirico M, D'Angelo A, Gianni C, Casadei C, Merloni F, De Giorgi U. Current State and Future Challenges for PI3K Inhibitors in Cancer Therapy. *Cancers (Basel)* 2023;**15**(3) doi 10.3390/cancers15030703.

9. Miller J, Armgardt E, Svoboda A. The efficacy and safety of alpelisib in breast cancer: A real-world analysis. *J Oncol Pharm Pract* 2022;**28**(5):1152-6 doi 10.1177/10781552221096413.

10. Salphati L, Heffron TP, Alicke B, Nishimura M, Barck K, Carano RA, *et al.* Targeting the PI3K pathway in the brain--efficacy of a PI3K inhibitor optimized to cross the blood-brain barrier. *Clin Cancer Res* 2012;**18**(22):6239-48 doi 10.1158/1078-0432.Ccr-12-0720.

11. Heffron TP, Ndubaku CO, Salphati L, Alicke B, Cheong J, Drobnick J, *et al.* Discovery of Clinical Development Candidate GDC-0084, a Brain Penetrant Inhibitor of PI3K and mTOR. *ACS Med Chem Lett* 2016;**7**(4):351-6 doi 10.1021/acsmedchemlett.6b00005.

12. Wen PY, Cloughesy TF, Olivero AG, Morrissey KM, Wilson TR, Lu X, *et al.* First-in-Human Phase I Study to Evaluate the Brain-Penetrant PI3K/mTOR Inhibitor GDC-0084 in Patients with Progressive or Recurrent High-Grade Glioma. *Clin Cancer Res* 2020;**26**(8):1820-8 doi 10.1158/1078-0432.CCR-19-2808.

13. Pascual J, Turner NC. Targeting the PI3-kinase pathway in triple-negative breast cancer. *Ann Oncol* 2019;**30**(7):1051-60 doi 10.1093/annonc/mdz133.

14. Zafar A, Wu F, Hardy K, Li J, Tu WJ, McCuaig R, *et al.* Chromatinized protein kinase C-theta directly regulates inducible genes in epithelial to mesenchymal transition and breast cancer stem cells. *Mol Cell Biol* 2014;**34**(16):2961-80 doi 10.1128/MCB.01693-13.

15. Bankhead P, Loughrey MB, Fernandez JA, Dombrowski Y, McArt DG, Dunne PD, *et al.* QuPath: Open source software for digital pathology image analysis. *Sci Rep* 2017;**7**(1):16878 doi 10.1038/s41598-017-17204-5.

16. Schmidt U, Weigert M, Broaddus C, Myers G. Cell Detection with Star-Convex Polygons: 21st International Conference, Granada, Spain, September 16–20, 2018, Proceedings, Part II. 2018:265-73 doi 10.1007/978-3-030-00934-2_30.

17. Wolf FA, Angerer P, Theis FJ. SCANPY: large-scale single-cell gene expression data analysis. *Genome Biol* 2018;**19**(1):15 doi 10.1186/s13059-017-1382-0.

18. Nolet C, Lal A, Ilango R, Dyer T, Movva R, Zedlewski J, *et al.* Accelerating single-cell genomic analysis with GPUs. 2022 doi 10.1101/2022.05.26.493607.

19. Schürch CM, Bhate SS, Barlow GL, Phillips DJ, Noti L, Zlobec I, *et al.* Coordinated Cellular Neighborhoods Orchestrate Antitumoral Immunity at the Colorectal Cancer Invasive Front. *Cell* 2020;**182**(5):1341-59.e19 doi 10.1016/j.cell.2020.07.005.

20. Heimes AS, Hartner F, Almstedt K, Krajnak S, Lebrecht A, Battista MJ, *et al.* Prognostic Significance of Interferon-gamma and Its Signaling Pathway in Early Breast Cancer Depends on the Molecular Subtypes. *Int J Mol Sci* 2020;**21**(19) doi 10.3390/ijms21197178.

21. Visvader JE, Lindeman GJ. Cancer stem cells in solid tumours: accumulating evidence and unresolved questions. *Nat Rev Cancer* 2008;**8**(10):755-68 doi 10.1038/nrc2499.

22. Mallick S, Duttaroy AK, Dutta S. The PIK3CA gene and its pivotal role in tumor tropism of triple-negative breast cancer. *Transl Oncol* 2024;**50**:102140 doi 10.1016/j.tranon.2024.102140.

23. Fultang N, Chakraborty M, Peethambaran B. Regulation of cancer stem cells in triple negative breast cancer. *Cancer Drug Resist* 2021;**4**(2):321-42 doi 10.20517/cdr.2020.106.

24. Hennessy BT, Gonzalez-Angulo AM, Stemke-Hale K, Gilcrease MZ, Krishnamurthy S, Lee JS, *et al.* Characterization of a naturally occurring breast cancer subset enriched in epithelial-to-mesenchymal transition and stem cell characteristics. *Cancer Res* 2009;**69**(10):4116-24 doi 10.1158/0008-5472.CAN-08-3441.

25. Li Y, Wang Z, Ajani JA, Song S. Drug resistance and Cancer stem cells. *Cell Commun Signal* 2021;**19**(1):19 doi 10.1186/s12964-020-00627-5.

26. Fan W, Li W, Li L, Qin M, Mao C, Yuan Z, *et al.* Bifunctional HDAC and DNMT inhibitor induces viral mimicry activates the innate immune response in triple-negative breast cancer. *Eur J Pharm Sci* 2024;**197**:106767 doi 10.1016/j.ejps.2024.106767.

27. Steenbrugge J, De Jaeghere EA, Meyer E, Denys H, De Wever O. Splenic Hematopoietic and Stromal Cells in Cancer Progression. *Cancer Res* 2021;**81**(1):27-34 doi 10.1158/0008-5472.CAN-20-2339.

28. Hao Y, He B, Wu L, Li Y, Wang C, Wang T, *et al.* Nuclear translocation of p85beta promotes tumorigenesis of PIK3CA helical domain mutant cancer. *Nat Commun* 2022;**13**(1):1974 doi 10.1038/s41467-022-29585-x.

29. Chen R, Ishak CA, De Carvalho DD. Endogenous Retroelements and the Viral Mimicry Response in Cancer Therapy and Cellular Homeostasis. *Cancer Discov* 2021;**11**(11):2707-25 doi 10.1158/2159-8290.Cd-21-0506.

30. Dardis GJ, Wang J, Simon JM, Wang GG, Baldwin AS. An EZH2-NF-kappaB regulatory axis drives expression of pro-oncogenic gene signatures in triple negative breast cancer. *iScience* 2023;**26**(7):107115 doi 10.1016/j.isci.2023.107115.

31. Huang J, Gou H, Yao J, Yi K, Jin Z, Matsuoka M, *et al.* The noncanonical role of EZH2 in cancer. *Cancer Sci* 2021;**112**(4):1376-82 doi 10.1111/cas.14840.

32. Gan L, Yang Y, Li Q, Feng Y, Liu T, Guo W. Epigenetic regulation of cancer progression by EZH2: from biological insights to therapeutic potential. *Biomark Res* 2018;**6**:10 doi 10.1186/s40364-018-0122-2.

33. Wang J, Yu X, Gong W, Liu X, Park K-S, Ma A, *et al.* EZH2 noncanonically binds cMyc and p300 through a cryptic transactivation domain to mediate gene activation and promote oncogenesis. *Nature cell biology* 2022;**24**(3):384-99.

34. Smale ST. Dimer-specific regulatory mechanisms within the NF-κB family of transcription factors. *Immunol Rev* 2012;**246**(1):193-204 doi 10.1111/j.1600-065X.2011.01091.x.

35. Wilkerson AD, Parthasarathy PB, Stabellini N, Mitchell C, Pavicic PG, Jr., Fu P, *et al.* Phase II Clinical Trial of Pembrolizumab and Chemotherapy Reveals Distinct Transcriptomic Profiles by Radiologic Response in Metastatic Triple-Negative Breast Cancer. *Clin Cancer Res* 2024;**30**(1):82-93 doi 10.1158/1078-0432.CCR-23-1349.

36. Blaye C, Darbo E, Debled M, Brouste V, Velasco V, Pinard C, *et al.* An immunological signature to predict outcome in patients with triple-negative breast cancer with residual disease after neoadjuvant chemotherapy. *ESMO Open* 2022;**7**(4):100502 doi 10.1016/j.esmoop.2022.100502.

37. De Angelis ML, Francescangeli F, La Torre F, Zeuner A. Stem Cell Plasticity and Dormancy in the Development of Cancer Therapy Resistance. *Front Oncol* 2019;**9**:626 doi 10.3389/fonc.2019.00626.

38. Dhanyamraju PK, Schell TD, Amin S, Robertson GP. Drug-Tolerant Persister Cells in Cancer Therapy Resistance. *Cancer Res* 2022;**82**(14):2503-14 doi 10.1158/0008-5472.Can-21-3844.

39. Marsolier J, Prompsy P, Durand A, Lyne AM, Landragin C, Trouchet A, *et al.* H3K27me3 conditions chemotolerance in triple-negative breast cancer. *Nat Genet* 2022;**54**(4):459-68 doi 10.1038/s41588-022-01047-6.

40. Godwin P, Baird AM, Heavey S, Barr MP, O'Byrne KJ, Gately K. Targeting nuclear factor-kappa B to overcome resistance to chemotherapy. *Front Oncol* 2013;**3**:120 doi 10.3389/fonc.2013.00120.

41. Francescangeli F, De Angelis ML, Rossi R, Cuccu A, Giuliani A, De Maria R, *et al.* Dormancy, stemness, and therapy resistance: interconnected players in cancer evolution. *Cancer Metastasis Rev* 2023;**42**(1):197-215 doi 10.1007/s10555-023-10092-4.

42. Tawara K, Oxford JT, Jorcyk CL. Clinical significance of interleukin (IL)-6 in cancer metastasis to bone: potential of anti-IL-6 therapies. *Cancer Manag Res* 2011;**3**:177-89 doi 10.2147/cmr.S18101.

43. Sanguinetti A, Santini D, Bonafè M, Taffurelli M, Avenia N. Interleukin-6 and pro inflammatory status in the breast tumor microenvironment. *World J Surg Oncol* 2015;**13**:129 doi 10.1186/s12957-015-0529-2.

44. Pu YS, Hour TC, Chuang SE, Cheng AL, Lai MK, Kuo ML. Interleukin-6 is responsible for drug resistance and anti-apoptotic effects in prostatic cancer cells. *Prostate* 2004;**60**(2):120-9 doi 10.1002/pros.20057.

45. Topper MJ, Vaz M, Marrone KA, Brahmer JR, Baylin SB. The emerging role of epigenetic therapeutics in immuno-oncology. *Nat Rev Clin Oncol* 2020;**17**(2):75-90 doi 10.1038/s41571-019-0266-5.

46. Chen Y, Zhu H, Luo Y, Tong S, Liu Y. EZH2: The roles in targeted therapy and mechanisms of resistance in breast cancer. *Biomed Pharmacother* 2024;**175**:116624 doi 10.1016/j.biopha.2024.116624.

47. Yomtoubian S, Lee SB, Verma A, Izzo F, Markowitz G, Choi H, *et al.* Inhibition of EZH2 Catalytic Activity Selectively Targets a Metastatic Subpopulation in Triple-Negative Breast Cancer. *Cell Rep* 2020;**30**(3):755-70.e6 doi 10.1016/j.celrep.2019.12.056.

48. Nie L, Wei Y, Zhang F, Hsu YH, Chan LC, Xia W, *et al.* CDK2-mediated site-specific phosphorylation of EZH2 drives and maintains triple-negative breast cancer. *Nat Commun* 2019;**10**(1):5114 doi 10.1038/s41467-019-13105-5.

49. Bachmann IM, Halvorsen OJ, Collett K, Stefansson IM, Straume O, Haukaas SA, *et al.* EZH2 Expression Is Associated With High Proliferation Rate and Aggressive Tumor Subgroups in Cutaneous Melanoma and Cancers of the Endometrium, Prostate, and Breast. *Journal of Clinical Oncology* 2006;**24**(2):268-73 doi 10.1200/jco.2005.01.5180.

50. Wang X, Hu B, Shen H, Zhou H, Xue X, Chen Y, *et al.* Clinical and prognostic relevance of EZH2 in breast cancer: A meta-analysis. *Biomed Pharmacother* 2015;**75**:218-25 doi 10.1016/j.biopha.2015.07.038.

51. Zong X, Wang W, Ozes A, Fang F, Sandusky GE, Nephew KP. EZH2-Mediated Downregulation of the Tumor Suppressor DAB2IP Maintains Ovarian Cancer Stem Cells. *Cancer Research* 2020;**80**(20):4371-85 doi 10.1158/0008-5472.Can-20-0458.

52. Lee ST, Li Z, Wu Z, Aau M, Guan P, Karuturi RK, *et al.* Context-specific regulation of NF-κB target gene expression by EZH2 in breast cancers. *Mol Cell* 2011;**43**(5):798-810 doi 10.1016/j.molcel.2011.08.011.

53. Yap TA, Winter JN, Giulino-Roth L, Longley J, Lopez J, Michot JM, *et al.* Phase I Study of the Novel Enhancer of Zeste Homolog 2 (EZH2) Inhibitor GSK2816126 in Patients with Advanced Hematologic and Solid Tumors. *Clin Cancer Res* 2019;**25**(24):7331-9 doi 10.1158/1078-0432.Ccr-18-4121.

54. Italiano A, Soria JC, Toulmonde M, Michot JM, Lucchesi C, Varga A, *et al.* Tazemetostat, an EZH2 inhibitor, in relapsed or refractory B-cell non-Hodgkin lymphoma and advanced solid tumours: a first-in-human, open-label, phase 1 study. *Lancet Oncol* 2018;**19**(5):649-59 doi 10.1016/s1470-2045(18)30145-1.

55. Thévenod F, Friedmann JM, Katsen AD, Hauser IA. Up-regulation of multidrug resistance P-glycoprotein via nuclear factor-kappaB activation protects kidney proximal tubule cells from cadmium- and reactive oxygen species-induced apoptosis. *J Biol Chem* 2000;**275**(3):1887-96 doi 10.1074/jbc.275.3.1887.

56. Braeuer SJ, Büneker C, Mohr A, Zwacka RM. Constitutively activated nuclear factor-kappaB, but not induced NF-kappaB, leads to TRAIL resistance by up-regulation of X-linked inhibitor of apoptosis protein in human cancer cells. *Mol Cancer Res* 2006;**4**(10):715-28 doi 10.1158/1541-7786.Mcr-05-0231.

57. Cantley LC. The phosphoinositide 3-kinase pathway. *Science* 2002;**296**(5573):1655-7 doi 10.1126/science.296.5573.1655.

FIGURES AND LEGENDS

Figure 1. Dual PI3K-mTOR blockade with paxalisib inhibits proliferation and migration, induces mesenchymal to epithelial transition, and reduces MIC signatures. (A) WST proliferation reagent was added to MDA-MB-231 cells pre-treated with PI3K and PI3K-mTOR inhibitors for 72 h in a dose-response design. Cell proliferation (%) was measured indirectly by the formation of formazan and the absorbance recorded at 450 nm. (B) Representative images from MDA-MB-231 cells scratched prior to treatment with paxalisib for 6 h, 12 h, and 18 h. Bar graph comparing the relative wound densities (%) observed for PI3K-mTOR inhibition at each time point, **** $p<0.0001$, versus vehicle, two-way ANOVA with Bonferroni's multiple comparisons test, n=8/group. Representative images and immunofluorescence analysis of (C) vimentin and (D) E-cadherin in 24 h paxalisib-treated MDA-MB-231 cells, **** $p<0.0001$, *** $p<0.001$ versus vehicle, unpaired *t*-test, n≥100 cells/group. (E) Flow cytometry analysis showing CD44:CD24 expression (%Vehicle) in 24 h paxalisib-treated MDA-MB-231 cells. (F) Immunofluorescence analysis of ALDH1, ABCB5, and Snail protein expression in 24 h paxalisib-treated MDA-MB-231 cells. ****, $p<0.0001$, versus vehicle, unpaired *t*-test, n≥100 cells/group. (G) Immunofluorescence analysis of nuclear and cytoplasmic NFκB p65, FOXQ1, NRF2, and NNMT protein expression in 24 h paxalisib-treated MDA-MB-231 cells, *, $p< 0.05$, ** $p< 0.01$, ***, $p<0.001$, ****, $p<0.0001$, versus vehicle, unpaired *t*-test, n≥100 cells/group. (H) Immunofluorescence analysis of IL-6 protein expression (%Total cells) in paxalisib-treated $ABCB5^{+}/EpCAM^{+}$ CTCs isolated from TNBC patients * $p<0.05$, versus vehicle, paired *t*-test, n=2/group. (I) qPCR analysis of viral mimicry-associated gene expression in 24 h paxalisib-treated MCF-7 iEMT cells, *$p<0.05$, versus vehicle, unpaired *t*-test, n=2/group. (J) Comparison of *GBP2* mRNA expression (%Vehicle) following 24 h PI3K and PI3K-mTOR

treatment in MCF-7 iEMT cells, versus vehicle, Dunnett's multiple comparisons test, n=2/group.

Figure 2. Paxalisib reduces primary tumor burden and metastasis with a favorable toxicity profile. (A) Treatment regimens using the BALB/c 4T1 TNBC breast cancer model (paxalisib with +/- anti-PD1, with or without Abraxane). (B) Primary tumor volumes (%Vehicle) and (F) weights of individual mice from each experimental group prior to harvest, * $p<0.05$, ** $p<0.01$, *** $p<0.001$, versus vehicle, Dunnett's, n=4-5/group. (C) (Left) Changes in liver inflammation and hepatocyte damage (metabolic and/or degeneration) were scored 1=mild, 2=moderate or 3=severe for each parameter, *$p<0.05$, **** $p<0.0001$, versus vehicle, Dunnett's, n=4-5/group. (Middle) Changes in lung weights and leukocytosis, * $p<0.05$, *** $p<0.001$, ****$p<0.0001$, versus vehicle, Dunnett's, n=4-5/group. (Right) Changes in spleen weights and spleen extramedullary hematopoiesis (EMH), * $p<0.05$, ** $p<0.01$, *** $p<0.001$, **** $p<0.0001$, versus vehicle, Dunnett's, n=4-5/group. (D) Paxalisib combined with αPD1 experiments using the BALB/c 4T1 i.v. metastasis breast cancer model. (E) Mouse body weights were monitored throughout the experiments. (F) Immunofluorescence images of CD45, vimentin, and SNAIL1 in MDA-MB-231 cells spiked into human healthy PBMCs. (G) CTCs were isolated using ScreenCell Cyto kits from mouse blood collected from the 4T1 i.v. metastasis model, followed by Giemsa staining. (H) Captured CTCs were counted on Cyto IS membranes. (I) Images of Indian ink-stained lungs highlighting metastases, including large protruding and small flat nodules and graph shows number of flat and protruding metastatic lung nodules, ** $p<0.01$, **** $p<0.0001$, versus vehicle, two-way ANOVA with Tukey's multiple comparisons test, n=2/group.

Figure 3. CODEX multiplexed imaging reveals changes in immune cell landscapes when of paxalisib is combined with immunotherapy. (A) Normalized expression of 23 proteins in 14 identified cell types. (B) Percentages of indicated cells types out of total cells in stromal, adaptive immune, innate immune, and tumor populations in αPD1 and Paxalisib+αPD1-treated tumors. (C) Differential location of stromal, tumor, adaptive, and innate cell populations in αPD1 and Paxalisib+αPD1-treated tumor tissues. (D) Representative images of neighborhoods mapped to tumor tissues from αPD1 and paxalisib+αPD1-treated tumors. (E) Quantification of neighborhood fraction in αPD1 and paxalisib+αPD1-treated tumors.

Figure 4. ***PI3K-mTOR inhibition enhances anti-tumor immune profiles in combination with immunotherapy.*** (A) NanoString nCounter cell abundance analysis of dendritic cell, cytotoxic cell, NK, and T and B cell immune populations from paxalisib +/- anti-PD1 treated tumors, n=3/group. (B) NanoString nCounter cell abundance analysis of TIL populations from paxalisib +/- anti-PD1-treated tumors, n=3/group. (C) NanoString nCounter gene expression levels of cytotoxicity-related cytokines, including IFN-gamma (IFN-γ) and Granzyme B (Gzmb), n=3/group. (D) NanoString nCounter cell abundance analysis of mast cell immune populations from paxalisib +/- anti-PD1-treated tumors, n=3/group. (E) Toluidine blue staining for mast cell detection in anti-PD1 and paxalisib + anti-PD1-treated tumors.

Figure 5. ***PI3K-mTOR inhibition targets p85β:H3K27Me3 switch.*** (A) Immunofluorescence images of p85β and H3K27Me3 in MDA-MB-231 cells. (B) Immunofluorescence analysis of p85β and H3K27Me3 nuclear intensity staining in paxalisib-treated MDA-MB-231 cells and MDA-MB-468 cells, * $p<0.05$, **** $p<0.0001$, versus vehicle, unpaired *t*-test.

Figure 6. ***PI3K-mTOR inhibition targets the dual role of EZH2.*** (A) qPCR analysis of *EZH2* mRNA expression in paxalisib-treated MDA-MB-231 cells ****, p<0.0001, unpaired *t*-test. (B) Immunofluorescence analysis of EZH2 nuclear intensity staining in paxalisib-treated MDA-MB-231 cells ****, p<0.0001, unpaired *t*-test. (C) Duolink analysis of the p85β:EZH2 interactions in paxalisib-treated MDA-MB-231 cells, ****, p<0.0001, unpaired *t*-test. (D) Duolink analysis of the NFκB:EZH2 interactions in paxalisib-treated MDA-MB-231 cells, ****, p<0.0001, unpaired *t*-test. (E) Overlap between the EZH2 bound upregulated and downregulated genes from the three comparisons (anti-PD1, paxalisib, and paxalisib + anti-PD1, relative to control). Differentially expressed genes were defined as log2Foldchange > 0.5 and p-value < 0.05. blue * indicated genes were also bound with H3K27me3. (F) Distribution of EZH2-bound genomic locations that are part of the nCounter Tumor 360 Signaling panel. (G) EZH2 and NFκB2 ChIP-seq tracks at IL-6 promoters in MDA-MB-231 cells.

Figure 7. Impact of dual PI3K-mTOR pathway inhibition in triple negative breast cancer. Mechanism 1. PI3K-mTOR blockade inhibits the resistant cancer cell populations (dormant tumor cells, CSCs, and persister cells), thereby overcoming resistance and reducing inflammation, including key pro-inflammatory cytokines such as IL-6. PI3K-mTOR inhibition also increases immune re-invigoration and activates viral mimicry signatures, making the cancer cells more immune visible. Using this biphasic approach of targeting resistance signatures and enhancing cancer immune visibility, when combined with immunotherapy or PARP inhibitors, PI3K-mTOR inhibition reduces primary tumor burden and metastases. **Mechanism 2.** *PI3K-mTOR blockade inhibits the dual role of EZH2.* PI3K-mTOR blockade (e.g., with paxalisib) acts upstream of EZH2, thereby targeting its dual role in resistance. PI3K-mTOR inhibitors potentially target EZH2 by two mechanisms. First, by

inhibiting p85β translocation into the nucleus, which diminishes the p85:EZH2 interaction, thereby inhibiting the catalytic repressive role of the epigenetic enzyme resulting in reduced H3K27 tri-methylation. By targeting upstream of EZH2, at the same time PI3K-mTOR blockade inhibits the non-catalytic inducible role of EZH2, thereby reducing NFκB signaling and downstream targets. Alternatively, PI3K-mTOR inhibition directly impacts EZH2 transcription, which in turn inhibits its dual catalytic and non-catalytic roles.

A
Proliferation
Paxalisib
p110α,β,δ,γ, mTOR
Dactolisib
p110α,β,δ,γ, mTOR
Apitolisib
PI3Kα/β/δ/γ, mTOR
Omipalisib
p110α/β/δ/γ,mTORC1/2
Dual PI3K-mTOR Inhibitors
2.5μM
0.4μM
0.6μM
0.3μM
LY294002
p110α,β,δ
Alpelisib
p110α
Idelalisib
p110 δ,γ
Wortmannin
PI3K
Single PI3K Inhibitors
25μM
133μM
92μM
>200μM
% Proliferation
Concentration (μM)
B
0 h
6 h
12 h
18 h
Vehicle
Paxalisib 2.5μM
Relative wound density (%)
Time (hrs)
****
C
Vimentin
Vehicle
Paxalisib
Vimentin cell intensity
D
E-cadherin
E-cadherin cell intensity
***
E
CD44/CD24 expression
CD44:CD24 ratio (% Vehicle)
↓67%
F
Resistance signature
ABCB5 cytoplasm intensity
ALDH1 cytoplasmic intensity
SNAI-1 nuclear intensity
G
Persister state
Nuclear
p65 NFκB
Nuclear p65 intensity
FOXQ1
Nuclear FOXQ1 intensity
NRF2
Nuclear NRF2 intensity
Cytoplasm
NNMT
Cytoplasmic NNMT intensity
Cytoplasmic FOXQ1 intensity
Cytoplasmic NRF2 intensity
H
IL-6 expression
IL-6+ CTCs (% Total cells)
Viral mimicry
I
Viral mimicry mRNA
Relative arbitrary copy number (normalised to ACTB/PPIA)
GBP2
IFIT1
IFIT2
IFIT3
IFIH1
IRF1
RSAD2
Control
J
GBP2 mRNA
GBP2 mRNA (% DMSO control)
Vehicle
Idelalisib
LY294002
Dactolisib
Paxalisib

Figure 1

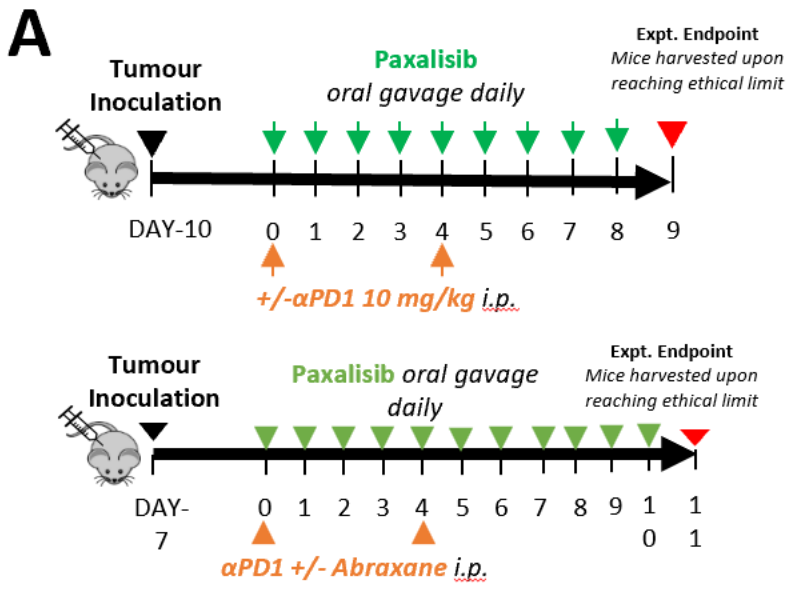

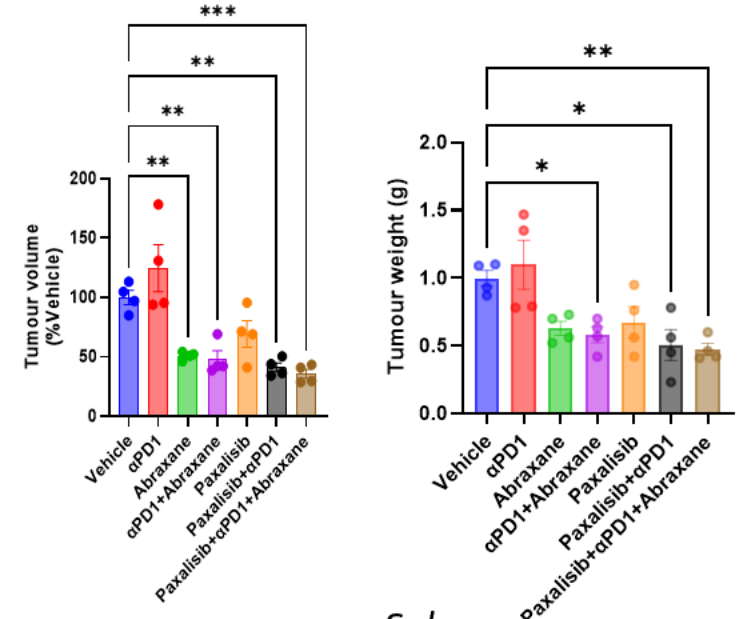

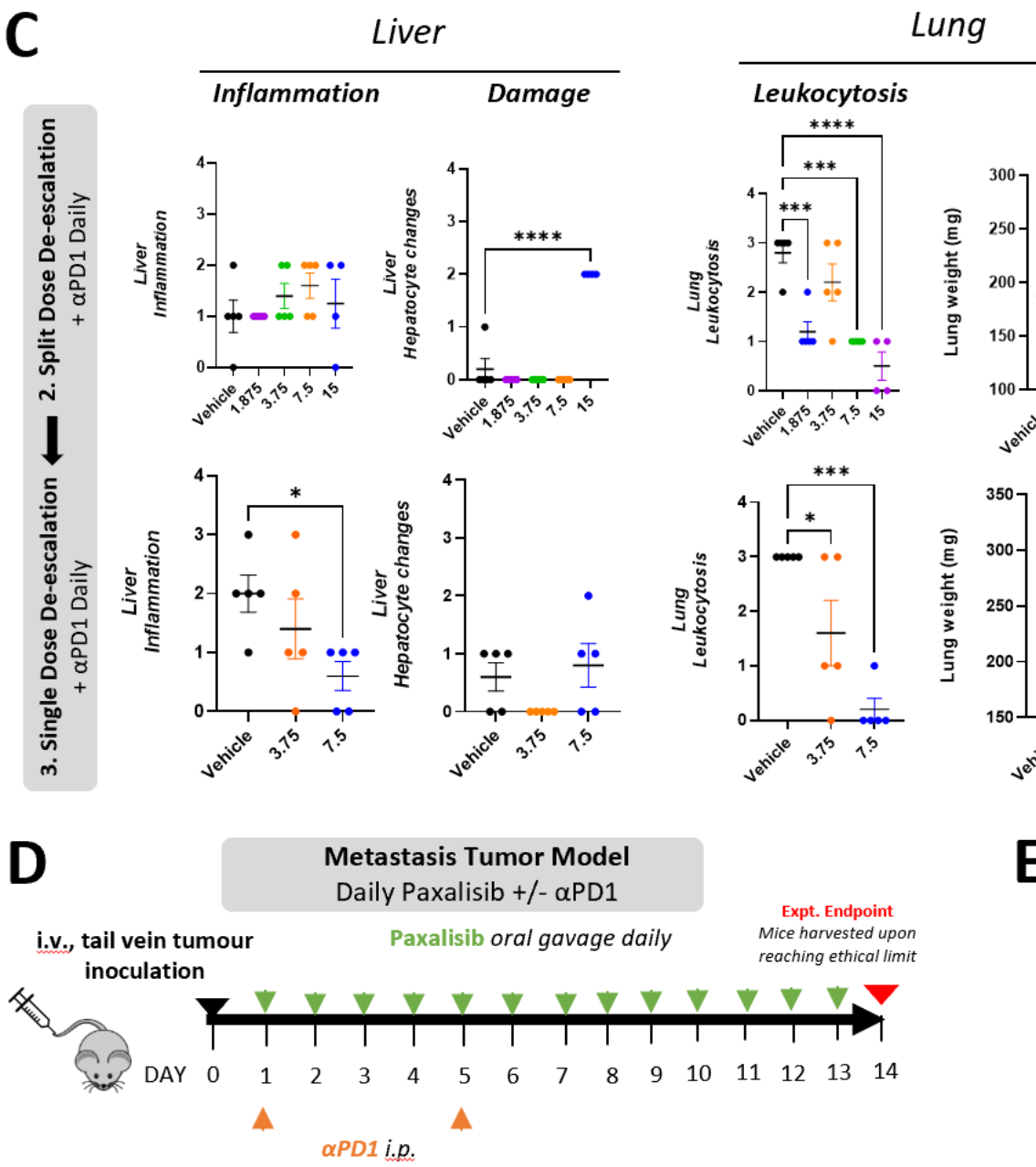

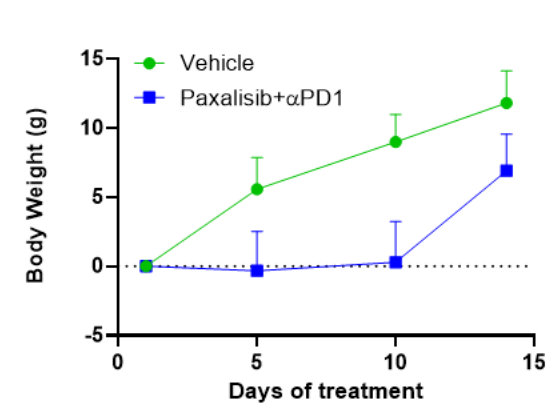

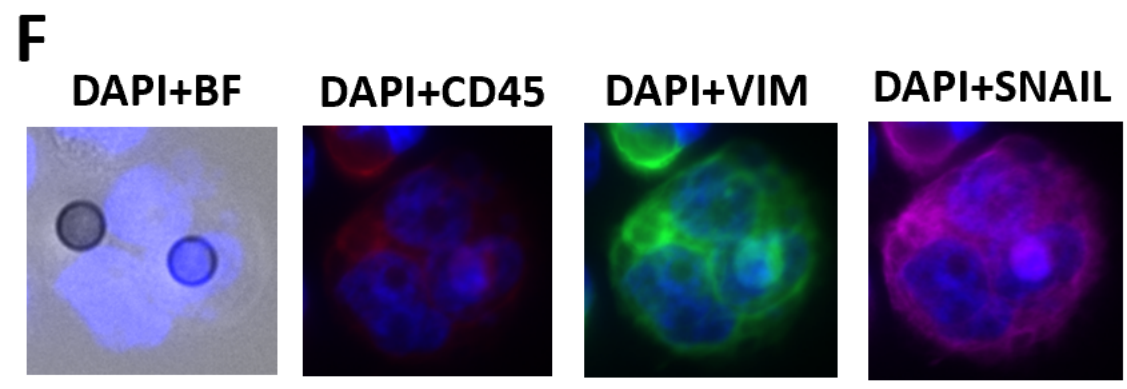

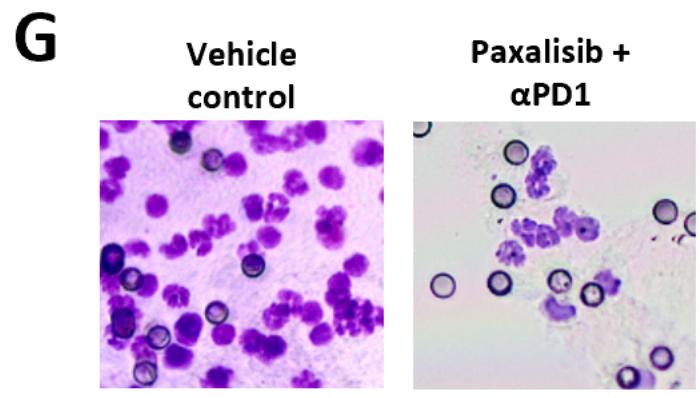

H

Treatment Group	Animal No#	Circulating Tumour Cells (CTCs) Counts
Vehicle Control	1	>1500
	2	>1500
	3	>1500
Paxalisib + αPD1	1	3
	2	12
	3	295

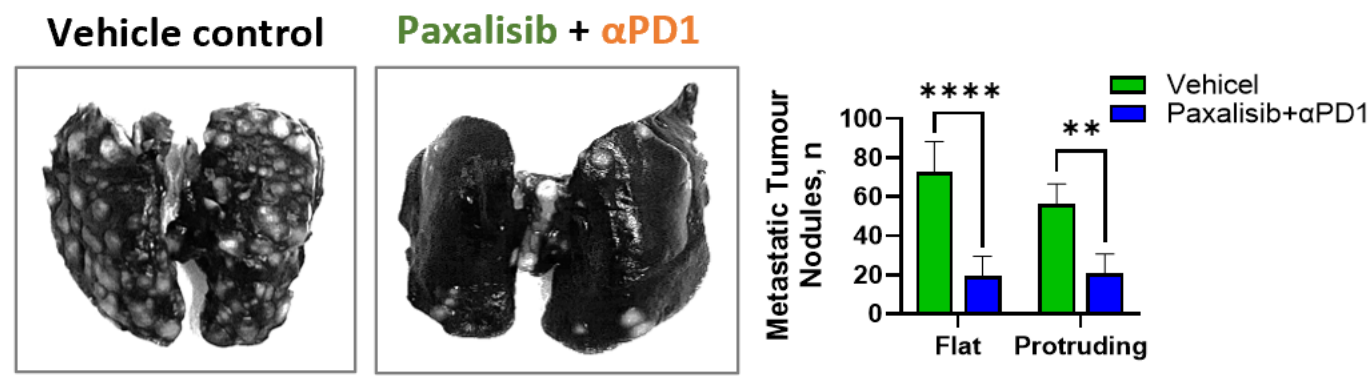

Figure 2

A

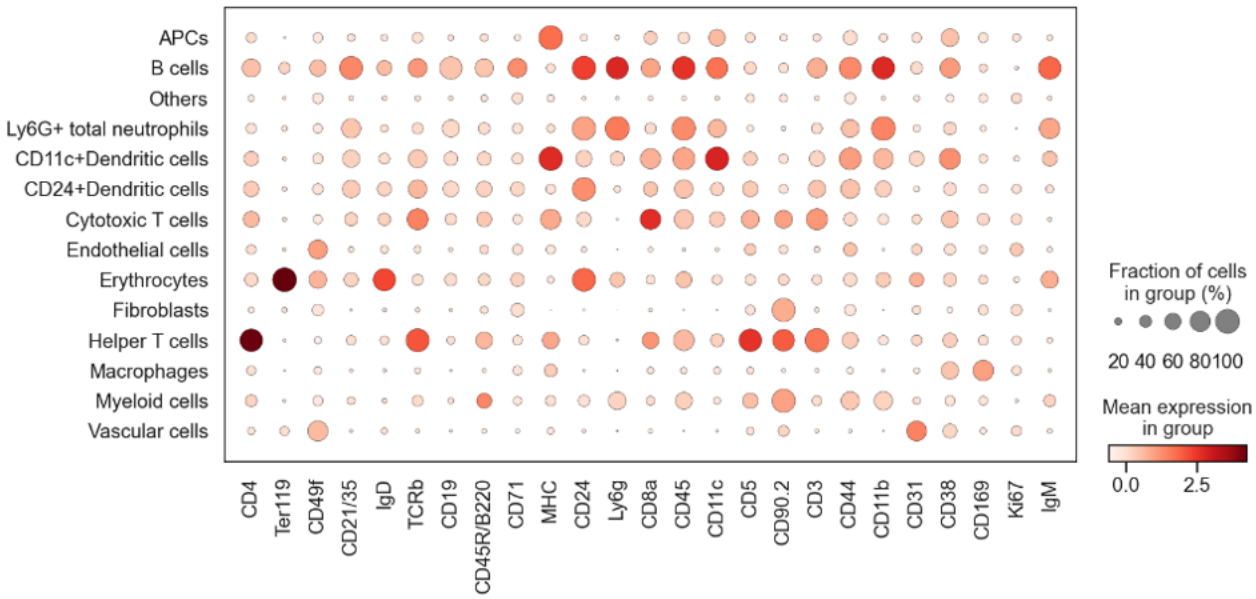

B

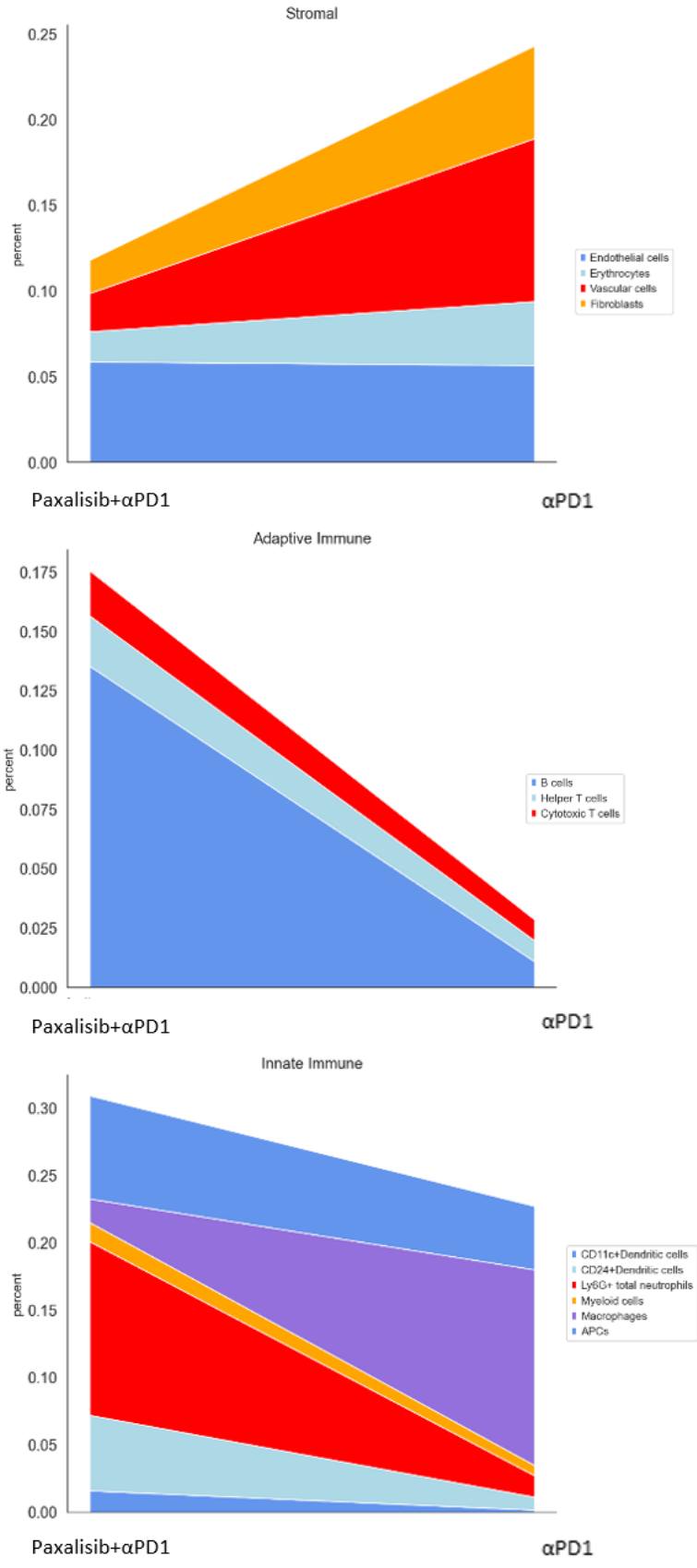

C

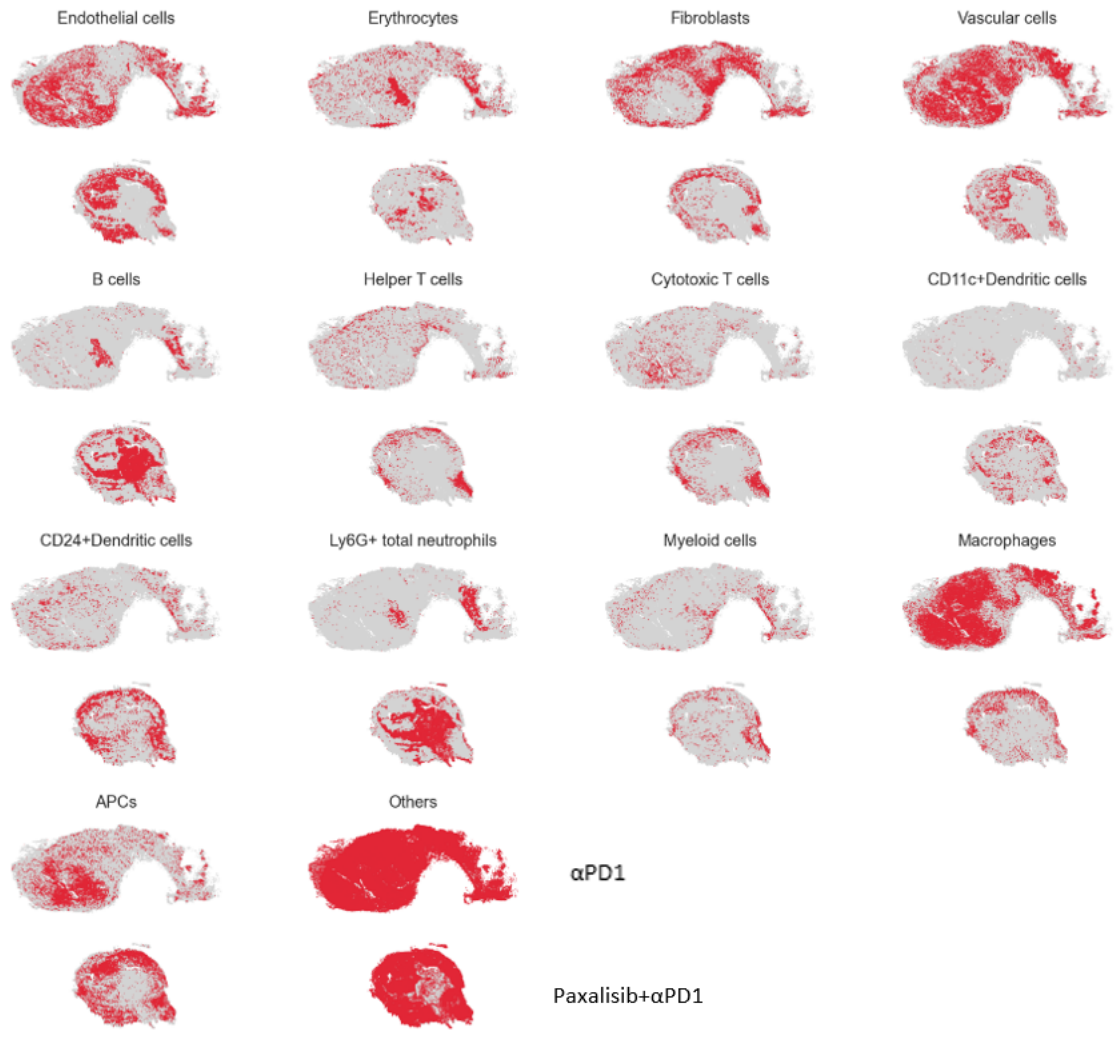

D

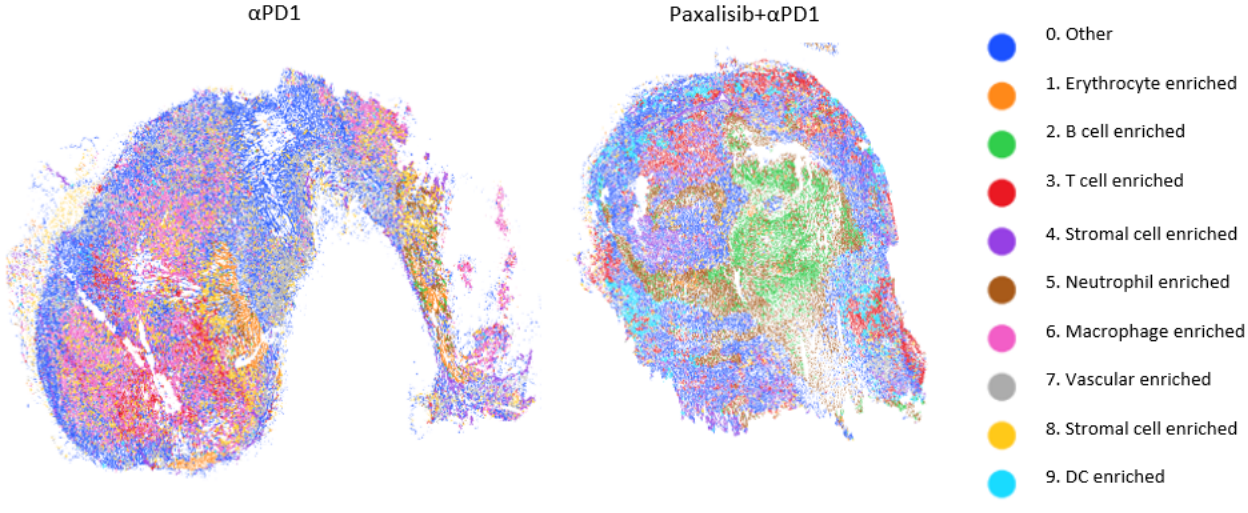

E

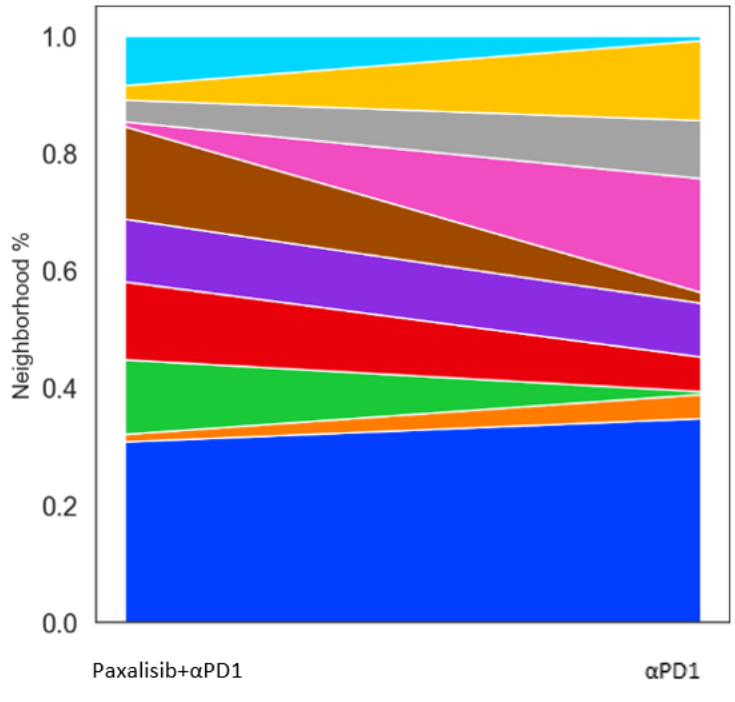

Figure 3

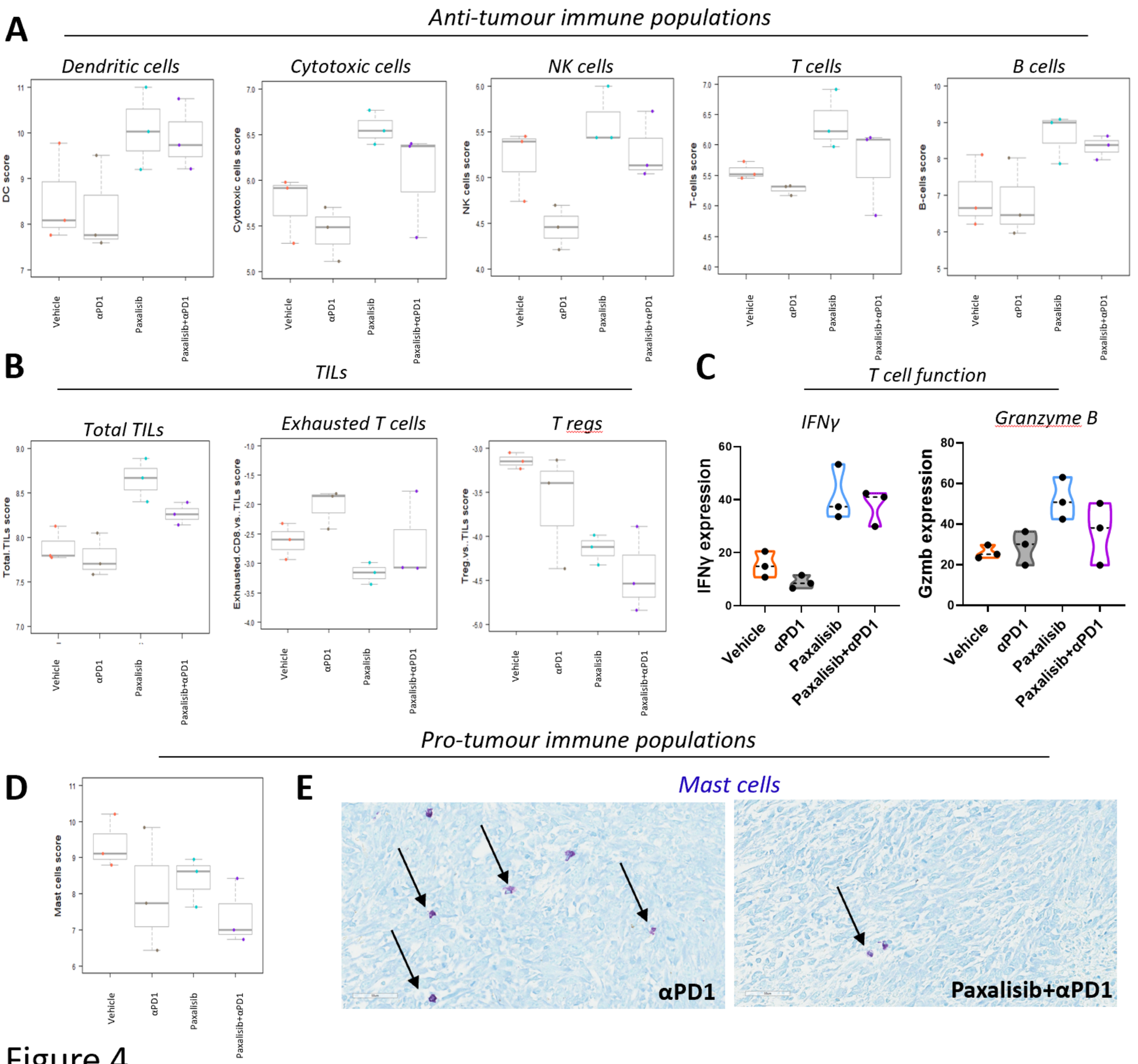
A
Anti-tumour immune populations
Dendritic cells
DC score
Cytotoxic cells
Cytotoxic cells score
NK cells
NK cells score
T cells
T-cells score
B cells
B-cells score
Vehicle
αPD1
Paxalisib
Paxalisib+αPD1
B
TILs
Total TILs
Total.TILs score
Exhausted T cells
Exhausted.CD8.vs..TILs score
T regs
Treg.vs..TILs score
C
T cell function
IFNγ
IFNγ expression
Granzyme B
Gzmb expression
D
Pro-tumour immune populations
Mast cells score
E
Mast cells
αPD1
Paxalisib+αPD1

Figure 4

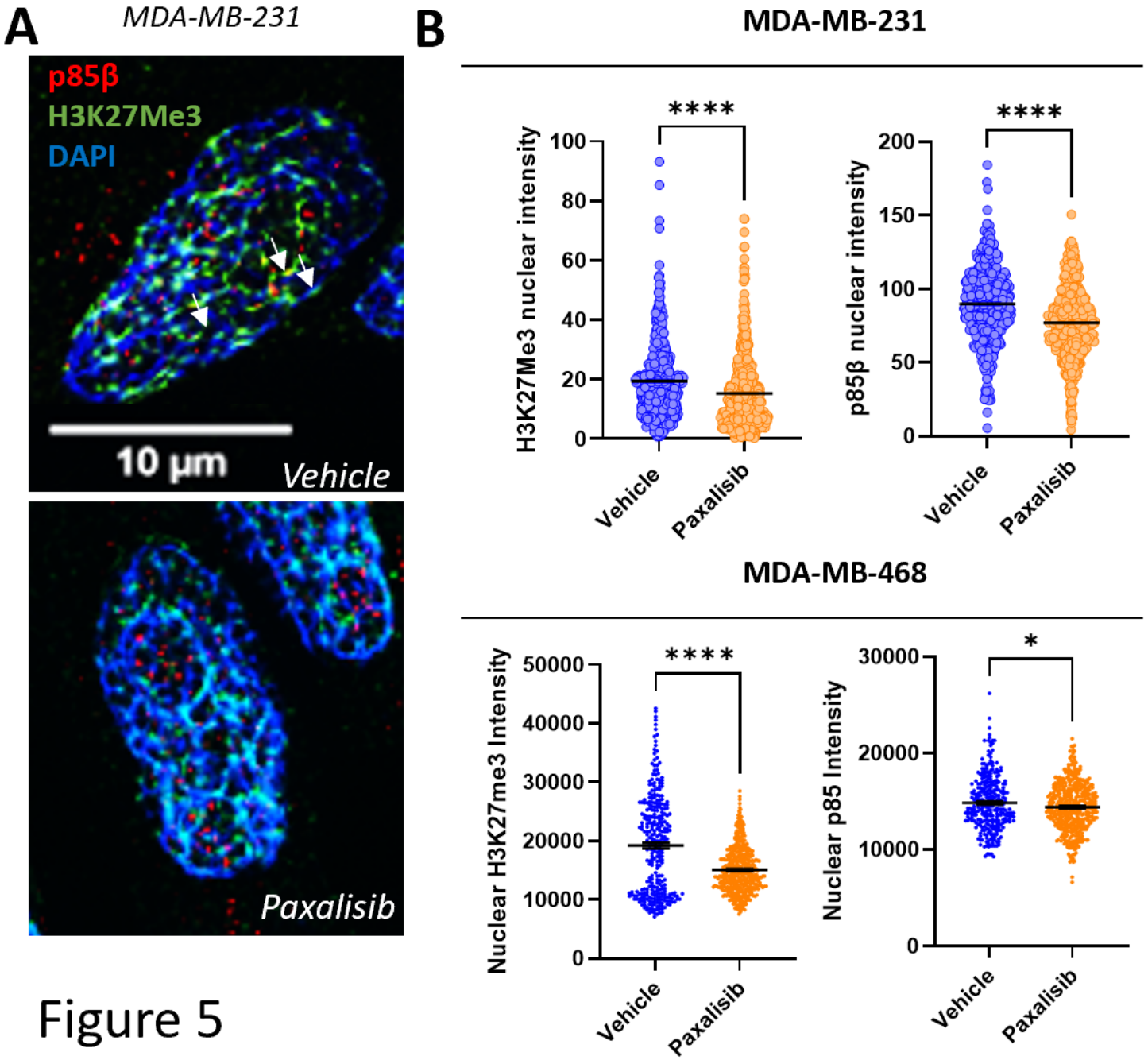
A
MDA-MB-231
p85β
H3K27Me3
DAPI
10 µm
Vehicle
Paxalisib
B
MDA-MB-231
H3K27Me3 nuclear intensity
p85β nuclear intensity
****
****
Vehicle
Paxalisib
MDA-MB-468
Nuclear H3K27me3 Intensity
Nuclear p85 Intensity
****
*

Figure 5

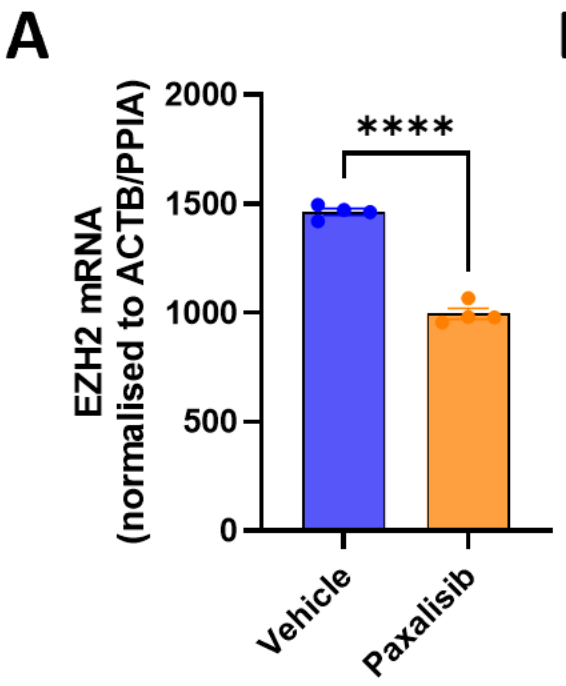

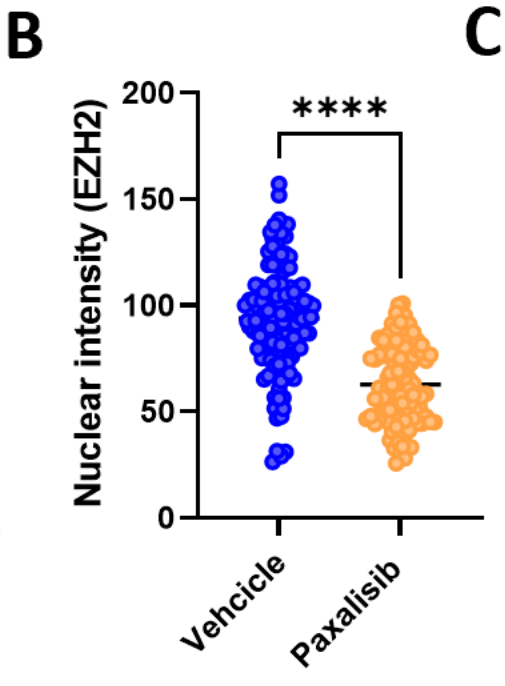

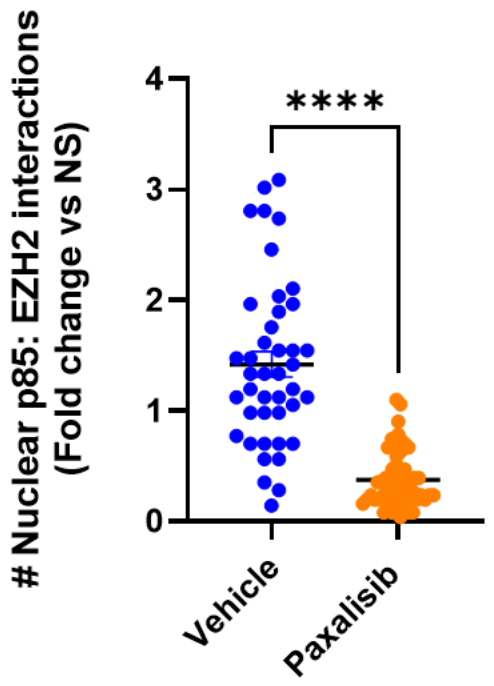

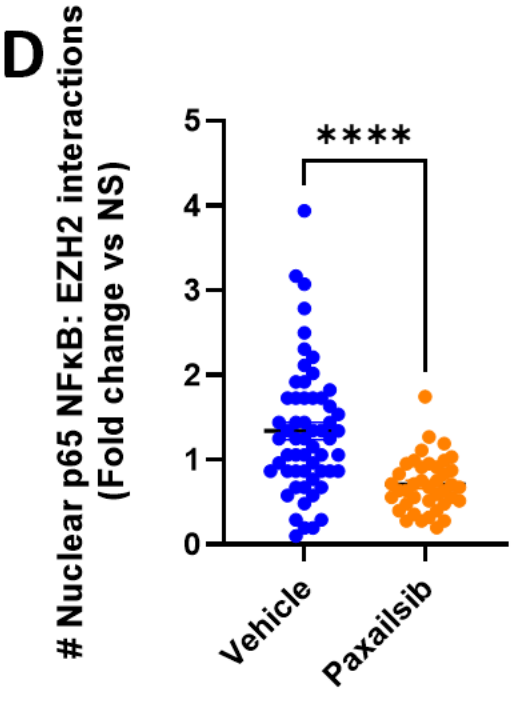

E

Upregulated DE with EZH2 binding

Paxalisib ONLY

Abcg2, Atf4, *Cd40, *Cdh1, *Csf2rb, Fas, Fcrlb, *Fgfbp1, *Gzmb, Icam1, *Il2ra, Jun, *Krt16, *Lck, *Nkg7, Ptgs2, Sfn, *Slc2a1

αPD1 ONLY

*Cd300a, *Csf3r, Epc1, Fpr1, Oas2, *Pik3r5, Thbs1

Paxalisib & Paxalisib+αPD1

*Ackr3, *Ccl4, Cd274, *Cd53, *Cdkn1a, Cxcr6, Hk2, Hmga1, *Il15ra, Irf1, *Mmp9, Mthfd2

αPD1 & Paxalisib+αPD1

*Ceacam1

Paxalisib+αPD1 ONLY

Adora2b, *Cd84, Fstl1, Pfkfb3, Serpine1, Stat3, *Vegfa

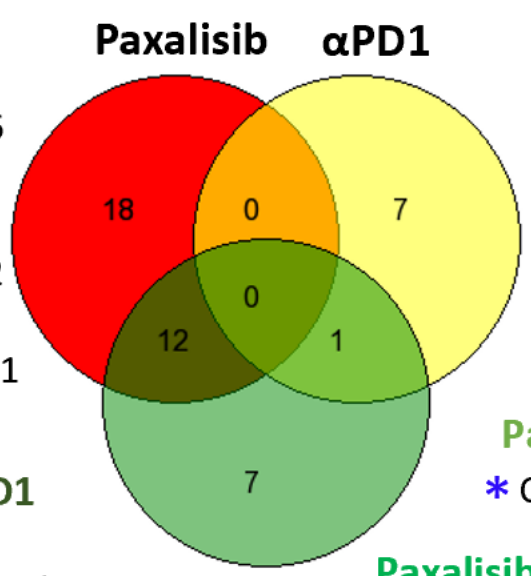

Downregulated DE with EZH2 binding

Paxalisib ONLY

*Cd33, *Cdh5, *Kdr, Lama4, *Notch3, Pdgfrb, Pik3r3

αPD1 ONLY

Ccnd1, *Cd247, Cxxc5, *Grap2, *Il21r, *Lat, *Mmp9, *Ncr1, Tapbp, Tns4

αPD1 & Paxalisib+αPD1

*Flt3, Sqle

Paxalisib & Paxalisib+αPD1

*Flt4, *Kit

Paxalisib+αPD1 ONLY

*Card11, *Cenpa, Fanca, Gtse1, Jup, Kif23, Ltbr, *Mki67, Nek2, Plk1, Rad54l, *Tpsab1, *Tpsb2

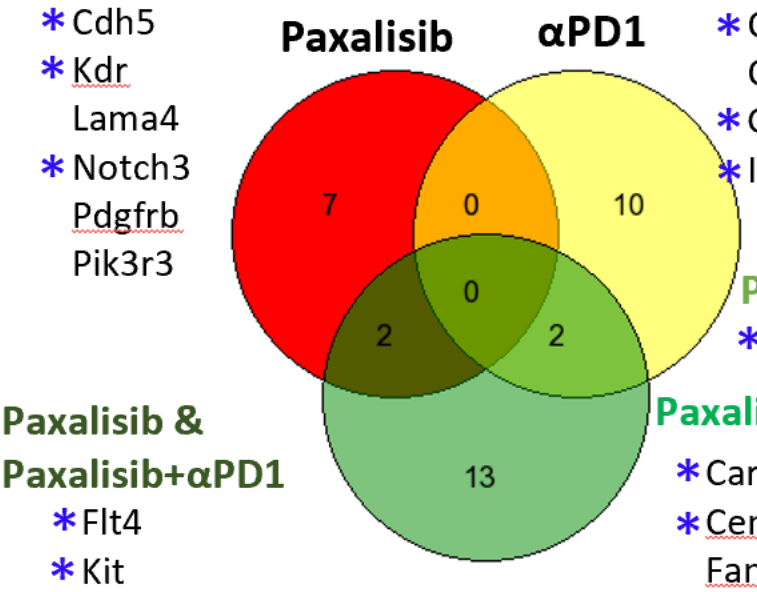

F

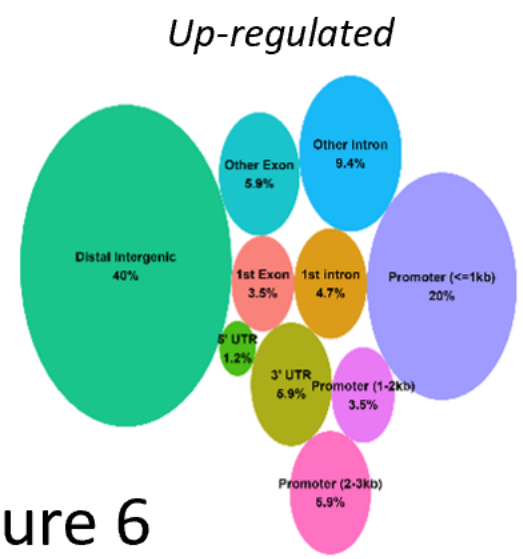

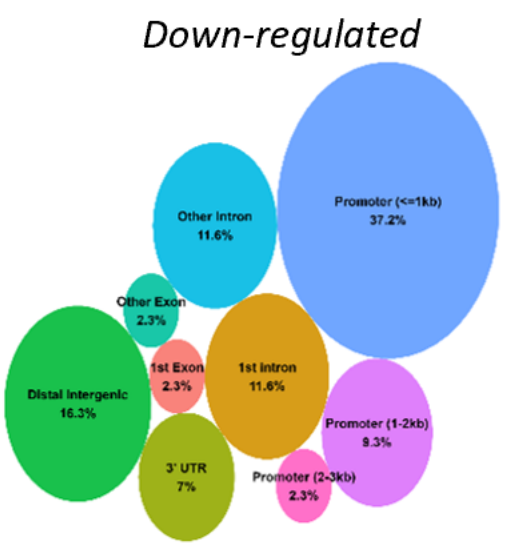

G

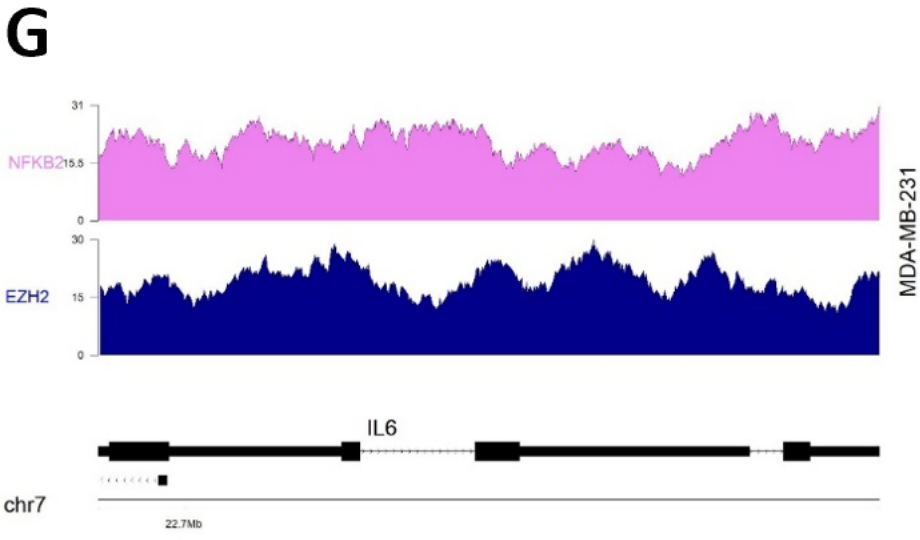

Figure 6

Mechanism 1

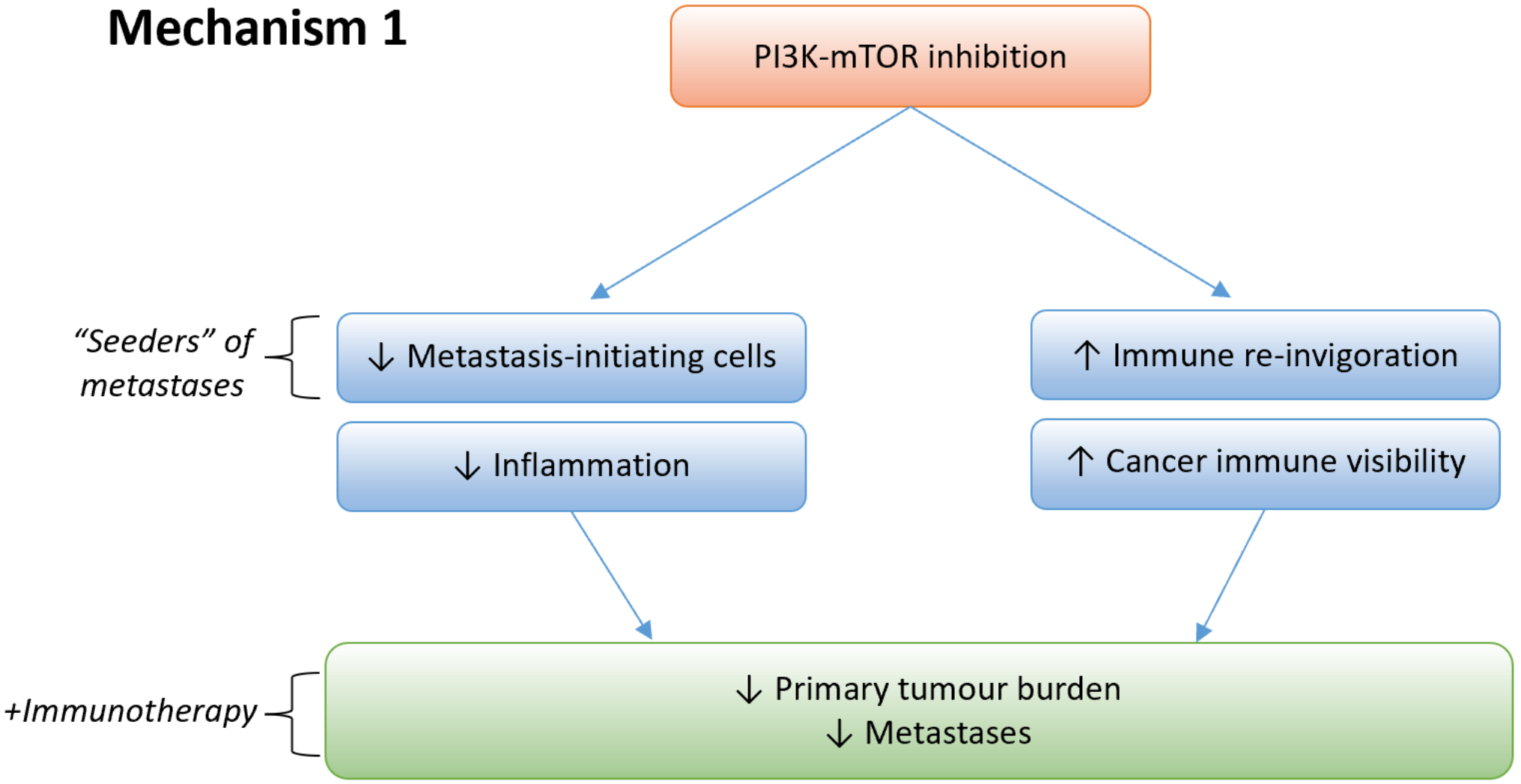

Mechanism 2

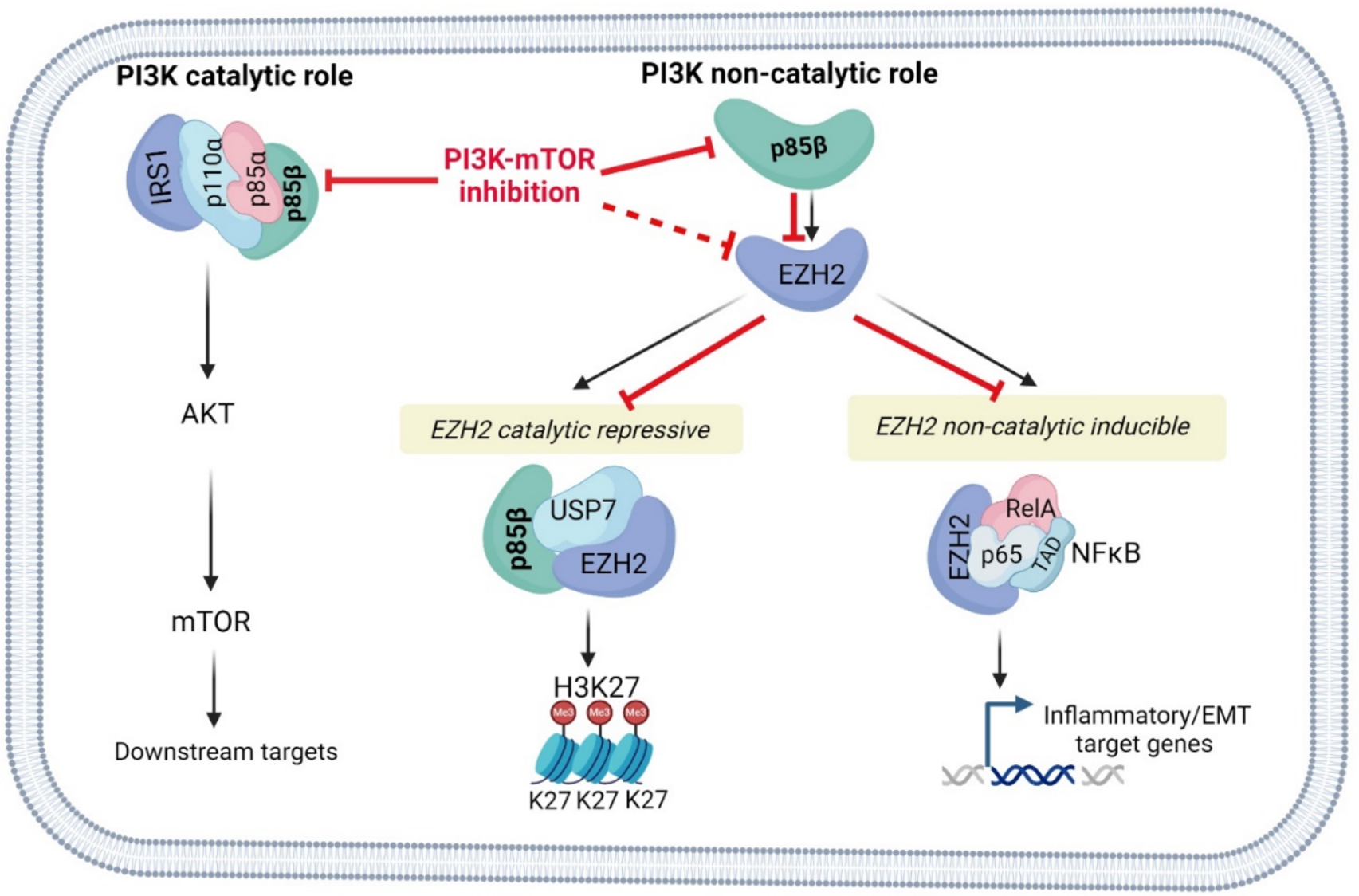

Figure 7